LANGMUIR

pubs.acs.org/Langmuir Article

Kinetic Control of Oxygen Interstitial Interaction with TiO_2(110) via the Surface Fermi Energy

Heonjae Jeong, Elif Ertekin, and Edmund G Seebauer*

Cite This: *Langmuir* 2020, 36, 12632−12648 Read Online

ACCESS | Metrics & More | Article Recommendations | Supporting Information

ABSTRACT: Atomically clean surfaces of semiconducting oxides efficiently mediate the interconversion of gas-phase O_2 and solid-phase oxygen interstitial atoms (O_i). First-principles calculations together with mesoscale microkinetic modeling are employed for TiO_2(110) to determine reaction pathways, assess appropriate rate expressions, and obtain corresponding activation energies and pre-exponential factors. The Fermi energy (E_F) at the surface influences the rate-determining step for both injection and annihilation of O_i. The barriers range between 0.72−0.82 eV for injection and 0.60−2.34 eV for annihilation and may be manipulated through intentional control of E_F. At equilibrium, the microkinetic model and first-principles calculations indicate that interconversion of O_i species in the first and second sublayers limits the rate. The effective pre-exponential factors for injection and annihilation are surprisingly low, probably resulting from the use of simple Langmuir-like rate expressions to describe a complicated kinetic sequence.

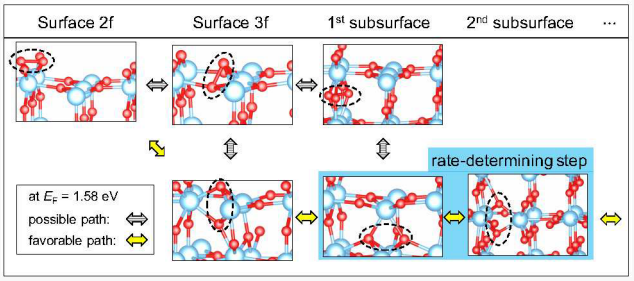

Downloaded via UNIV ILLINOIS URBANA-CHAMPAIGN on November 23, 2020 at 19:55:44 (UTC).
See https://pubs.acs.org/sharingguidelines for options on how to legitimately share published articles.

INTRODUCTION

Atomically clean surfaces of semiconducting oxides efficiently mediate the movement of oxygen between gas-phase O_2 and the solid.[1,2] This mediation entails not only desorption and adsorption of O_2, but also injection and annihilation of oxygen interstitial atoms (O_i). O_i diffuses readily within many oxides, and serves as a principal intermediate by which the lattice and extended defects equilibrate in response to changes in temperature and pressure. The kinetic processes surrounding desorption and adsorption on oxides have been examined for many years, but corresponding investigations of injection and annihilation remain spotty.[3−6] These latter processes operate in loose analogy to desorption and adsorption as shown in Figure 1, and hypotheses about the rate expressions have sometimes made explicit use of this analogy.[7,8] The accuracy of this analogy awaits confirmation, however, not only to understand the underlying principles, but also to harness them for technological purposes in semiconductors.[9]

Most experimental measurements of defect injection or annihilation monitor the temporal evolution of an isotopic label's concentration profile in the near-surface bulk, with injection kinetics inferred through a mesoscale model. The best models incorporate microkinetic rate expressions for injection and annihilation of point defects at the surface, site-to-site diffusional hopping within the bulk, and sequestration in bulk reservoirs such as the lattice and extended defects. For oxides, comprehensive treatments include point defects of both anions and cations. The models employ optimization schemes to determine the constituent parameters (e.g., activation energies and pre-exponential factors) that best fit the experimental data.

Functional forms for some kinetic processes such as site hopping rest upon firm experimental and computational foundations. However, the rate expressions for injection and annihilation typically represent educated guesses because the atomic mechanisms remain incompletely understood. First-principles calculations by density functional theory (DFT) offer a basis for choosing among several possible reaction pathways, developing appropriate rate expressions, and interpreting the parameters derived from microkinetic modeling. Such explicit synergy between DFT and microkinetic modeling has been attempted only recently in the case of O_i in rutile TiO_2 near chemical equilibrium. That work focused only upon mesoscale diffusion[10] or thermodynamics of the intermediate states of O_i at or near the surface.[11]

The present work broadens the scope of prior studies by using related methods to examine the barriers for elementary steps governing injection and annihilation of O_i at TiO_2(110). Several surprising discoveries emerge. For example, the Fermi energy (E_F) at the surface regulates the rate-determining step for both injection and annihilation. As E_F moves between the

Received: July 25, 2020
Revised: October 1, 2020
Published: October 16, 2020

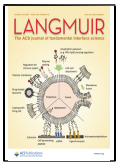

© 2020 American Chemical Society

https://dx.doi.org/10.1021/acs.langmuir.0c02195
Langmuir 2020, 36, 12632−12648

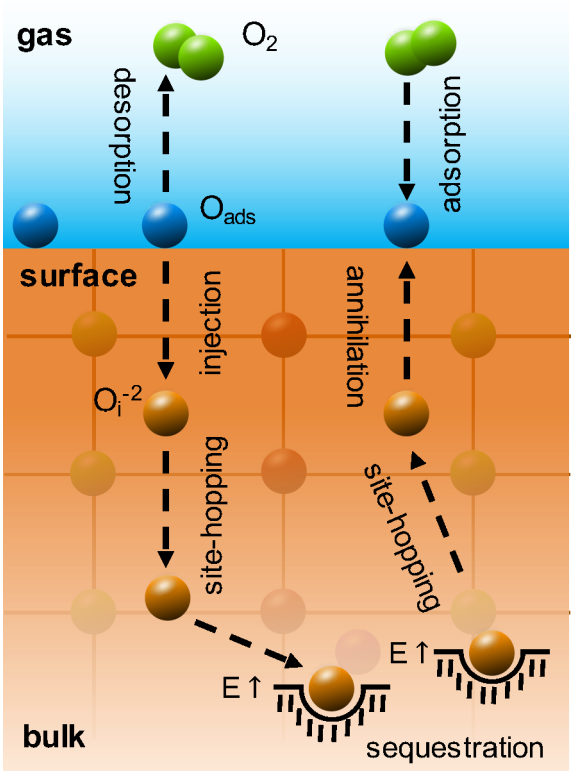

Figure 1. Schematic diagram of oxygen exchange between O_2 gas and the rutile TiO_2 bulk mediated by O_i^{-2}, showing the main governing processes and illustrating certain analogies between some of them. For injection and desorption, the surface loses adsorbate and the rate expressions have identical functional forms. For annihilation and adsorption, the surface gains adsorbate. However, the rate expressions differ slightly because the flux from the bulk originates from diffusive site-to-site hopping, whereas that from the gas originates from free-particle translation. Sequestration immobilizes O_i^{-2} either temporarily or permanently during an experiment, depending upon the energy E required for liberation from the sequestration site. For TiO_2 in this work, extended defects serve as the main sequestration site.

edges of the valence and conduction bands, the injection barrier varies between 0.72 and 0.82 eV, and the annihilation barrier varies between 0.60 and 2.34 eV. Consequently, the limiting steps for both injection and annihilation can be manipulated through intentional control of the surface E_F. Under the experimental conditions (T = 650−800 °C with oxygen partial pressures between 5×10^{-6} and 6×10^{-5} Torr and E_F = 1.58 eV), the effective activation energy for injection lies near 1.2 eV, and the effective pre-exponential factor is surprisingly low near 10^5 s^{-1}. The pre-exponential's behavior mirrors that seen for titanium interstitial injection into rutile,[8] and probably results from using simple Langmuir-like rate expressions to describe a rather complicated kinetic sequence.

METHODS

Self-diffusion rates of oxygen are often measured by exchange with a gaseous ambient of isotopically labeled $^{18}O_2$. In the presence of a surface that is not passivated by foreign adsorbate, the evolution of an oxygen self-diffusion profile is mediated by O_i and is governed by the kinetics of (1) surface injection and annihilation, (2) bulk site-hopping, and (3) immobilization by sequestration in a bulk reservoir such as the lattice or extended defects. Figure 1 illustrates these processes.

The original oxygen self-diffusion profiles have been detailed previously,[1,2] and originated from gas−solid exchange experiments wherein single crystal rutile TiO_2(110) specimens were annealed at 650−800 °C in isotopically labeled oxygen gas ($^{18}O_2$) with oxygen partial pressures between 5×10^{-6} and 6×10^{-5} Torr. Before exposure to the isotopic label, specimens were annealed in natural abundance oxygen for 4 h at the temperature chosen for subsequent diffusion. This procedure yields an atomically clean surface as well as the equilibration of oxygen point defect concentrations. Isotopic concentrations vs. depth were measured by ex-situ time-of-flight secondary ion mass spectrometry.

Mesoscale Modeling. Microkinetic analysis of isotopic self-diffusion profiles to determine the kinetic parameters employed a numerical simulator (FLOOPS)[12] that solves coupled continuum mass balance equations for the relevant defects, together with an optimization algorithm that finds a set of parameter values (mostly activation energies and pre-exponential factors) yielding the best fit to a family of experimental profiles.[7,8,13] The optimization algorithm employs a weighted sum of squared errors whose objective function is iteratively minimized to a tolerance of 0.05%. The profile simulator assumes specific functional forms for the elementary kinetic expressions describing the diffusion-reaction network. Microkinetic models for rutile TiO_2 in the presence of a nearby surface have been formulated previously,[7,8,14] and validation efforts have yielded progressively increasing fidelity to experimental results. Because O_i in TiO_2 is charged, defect motion near the surface includes a drift component if built-in charge induces formation of a surface space charge layer. Such effects manifest in TiO_2 isotopic exchange experiments as a narrow pile-up region next to the surface, but only a small fraction of the injected label is affected and the effects can be decoupled and modeled separately[15,16] from the deeper-bulk profiles examined here.

The present work progresses beyond previous versions through an improved representation of the bandgap (E_g) of rutile described below, together with a much broader range of initial parameter values employed for optimizing the objective function. Earlier implementation of the optimization explored a region near the solid's Debye frequency (~1×10^{13} s^{-1}) as the pre-exponential factor of O_i injection, and corresponding parameter sensitivity analysis[17,18] exhibited no significant effects. However, such implementations occasionally find optima that are only local rather than global, especially if some of the parameters lie far from the expected region.

The value of bandgap (E_g) propagates with a strong exponential dependence into the equilibrium concentrations of both O_i and the titanium interstitial Ti_i, meaning that even modest variations in E_g can induce significant changes in the parameter values returned by the optimization. Several reports in the literature document the dependence of E_g for rutile upon temperature T, usually decreasing according to the phenomenological linear relation and given by eq 1

$$E_g = E_0 - \beta T \tag{1}$$

where E_0 is a bandgap at 0 K and β is a positive quantity on the order of 10^{-3} eV/K. However, these reports either disagree with each other or cover different temperature regimes.

To mitigate this problem, the present work employed eq 1 together with composite values of E_0 and β obtained through maximum likelihood estimation.[19] This approach yields an averaged value of the parameters, with each literature report weighted in inverse proportion to its likely uncertainty. Application of this method yielded E_0 = 3.07 ± 0.08 eV and $\beta = (0.7 \pm 0.11) \times 10^{-3}$ eV/K. At the temperatures of interest, these values lead to a bandgap that is 0.15−0.20 eV larger than in the earlier microkinetic models of refs 8 and 14.

Results from the microkinetic model were compared to those from a different mesoscale approach based upon analytical profile-by-profile determination of the slopes and intercepts in semilogarithmic plots.[20] The approach makes few assumptions about the kinetic mechanisms at play, and yields parameters representing composites of elementary-step rate constants. This approach works well when the profiles evolve in certain asymptotic kinetic limits. At short times during which the mobile intermediate transporting the label becomes immobile at

https://dx.doi.org/10.1021/acs.langmuir.0c02195
Langmuir 2020, 36, 12632−12648

sequestration sites and remains there for the duration of the experiment, the profile slope yields the mean diffusion length λ while the intercept yields the net injection flux F. These two composite parameters yield a third useful profile metric, the effective diffusivity D_{eff}.[1,2]

As discussed elsewhere,[1,2] the short-time assumption's validity is supported by examination of the profile shapes, which should be straight lines when plotted semilogarithmically. The original profiles employed here satisfy that criterion. That criterion does not provide sufficient evidence, however, as many repeated sequestration and liberation events of O_i also yield essentially linear profiles near the surface in semilogarithmic plots. Constraints on the ability of secondary ion mass spectrometry (SIMS) to resolve small concentration changes, together with finite practicable times for profiling, permit capture of only small fractions of the total ^{18}O profiles to depths of a few hundred nanometers. As described in a subsequent section, however, parameters determined in the present experiments from the microkinetic modeling provide strong evidence for the short-time limit's validity.

The interstitialcy mechanism for diffusion for oxygen in rutile TiO_2 transpires via O_i in a symmetric split geometry[10] in which two oxygen atoms symmetrically share the site normally occupied by a lattice oxygen atom. However, the ^{18}O comprises on the order of only 1% of the total oxygen concentration at any point in the profile. This low percentage, together with the symmetry of the split geometry, implies that the hopping diffusion coefficient describing must be scaled by a statistical factor that differs for ^{16}O and ^{18}O. There are three possible ways ^{16}O and ^{18}O may be paired for a split configuration corresponding to O_i: two ^{16}O's, one ^{16}O and one ^{18}O, and two ^{18}O's. With ^{18}O comprising only about 1% of the total oxygen at any point, these three possibilities should exist in a ratio of roughly $1{:}10^{-2}{:}10^{-4}$. Thus, a ^{16}O usually pairs with another ^{16}O at a split defect. But ^{18}O usually pairs with ^{16}O, and each atom has an equal chance of making the next hop. So the chance that ^{18}O becomes temporarily immobilized as a lattice atom is 50% after one hop, 75% after two hops, 87.5% after three hops, and so on. Temporary immobilization, therefore, effectively occurs after only a couple of hops—much shorter than the distance between extended defects that comprise the primary sequestration sites. Once immobilized in the lattice, the ^{18}O must wait for another O_i (of either isotope) to come by and liberate it. The pairing of two ^{18}O atoms in the split O_i configuration happens so infrequently that we neglect that possibility, meaning that $^{18}O_i$ effectively refers to ^{18}O paired with ^{16}O.

If D_{hop} denotes the hopping diffusivity of O_i in a hypothetical single-isotope solid (or equivalently, computed by DFT), then the statistical effects imply an effective hopping diffusivity for ^{18}O to $[^{18}O_i]/([^{18}O_i]+[^{16}O_i])D_{hop} \approx 0.01D_{hop}$, while the corresponding effective hopping diffusivity for ^{16}O will be $[^{16}O_i]/([^{18}O_i]+[^{16}O_i])D_{hop} \approx 0.99D_{hop}$. Such statistical effects do not occur for a vacancy mechanism, or for an interstitial mechanism wherein the mobile species does not pair with a lattice atom. A previous first-principles study of ours[10] determined D_{hop} to be a factor of 150 above the reported microkinetic value for ^{18}O;[7,14] accounting for this statistical effect brings the two values into excellent agreement with each other.

DFT Calculations. First-principles DFT simulations were employed as detailed previously to yield reaction pathways and activation energies for elementary kinetic steps.[11] Although DFT is beginning to yield reliable values for pre-exponential factors[10] for solid-state diffusion, such computations were not performed here. The degree of confidence with which DFT rate constants may be compared to those from microkinetic analysis has been detailed elsewhere.[10]

The DFT calculations[21,22] carried out here employed the Vienna Ab-Initio Simulation Package (VASP)[23,24] with projector augmented wave (PAW)[25] pseudopotentials and the generalized gradient approximation (GGA)[26] to the exchange-correlation functional of Perdew-Burke-Eznerhof (PBE).[26] The slab geometry and simulation settings for the plane-wave energy cutoff and Brillouin zone sampling match those in a previous study.[11] The initial surface geometry was taken to be the (1×1) rutile $TiO_2(110)$ structure that prevails at the experimental condition of about T = 700 °C and $P_{O_2} = 10^{-5}$ Torr.[1,2,7,14] The climbing image nudged elastic band (NEB) method[27] was employed to calculate minimum energy pathways and their kinetic barriers. The spring constant was −5 eV/Å, and atomic positions were relaxed until the maximum total force on any atom fell below 0.05 eV/Å. The well-known O_2 overbinding issue in DFT-GGA[28] was corrected according to the methods of ref 29 in the DFT-computed total energy of O_2. Implementation details for TiO_2 appear elsewhere.[10]

Prior experimental[14] and computational[10,11] work indicates that O_i exists as a −2 ion in n-type rutile TiO_2. To obtain this charged state in DFT, an artificial O vacancy (V_O) was introduced at the back of the slab, from which adsorbed O or bulk O_i can draw electrons as necessary in order to charge. The approach allows determination of configuration energies at arbitrary Fermi energy, accounting for charge exchange between adsorbed O or bulk O_i with the semiconductor bulk. The details of the approach have been described elsewhere in the literature.[30,31] Charged states of the defect were determined by examination of the Bader charge on the relevant oxygen atoms and inspection of electron occupation in the density of states for the slab. Energies of charged defects as a function of E_F were determined as described elsewhere.[11]

To compare computed energy profiles to experiments, the experimental Fermi energy should be established. E_F in the bulk was not measured directly in the experiments but was instead computed from concentrations of point defects acting as donors (Ti_i^{4+}) and acceptors (O_i^{2-}) in the microkinetic model. At the temperatures and pressures of interest, this approach yielded E_F = 1.58 eV above the valence band maximum (VBM). The surface Fermi energy was set equal to that in the bulk based on the assumption of no band bending. Previous studies of oxygen adsorption on rutile have indicated that surface defects created by annealing generally induce downward band banding of 0.2−0.3 eV, while oxygen adsorption causes upward band bending by a similar amount.[32,33] Indeed, oxygen adsorption on initially reduced single-crystal $TiO_2(110)$ yields a flat band condition,[32] thereby supporting the assumption made here.

The use of GGA-PBE may affect the results in terms of both the material's bandgap and the positioning of some defect levels within the bandgap, because of the underestimated bandgap and the tendency of PBE to delocalize electrons. We employed several approaches based on ref 34 to estimate corrections for finite-size effects, underestimated bandgap, and positions of defect levels, and find that these put our predictions within 0.2 eV of results from hybrid functional DFT. We also used PBE+U approach to analyze the sensitivity of the density of states and the charge transfer to the value of U. The analysis is detailed in our recent work.[11]

RESULTS

Microkinetic Parameters. Table 1 shows thermodynamic and kinetic parameters and confidence intervals from the microkinetic model. Although many parameters in Table 1 remain close to those obtained from previous microkinetic work,[7,8,14] several differ appreciably. In particular, the injection activation energy E_{inj} decreases by nearly a factor of 2 from 2.4 to 1.28 eV, and the corresponding pre-exponential factor ν_{inj} decreases by almost 8 orders of magnitude to about 10^5 s^{-1}. Several other parameters exhibit more modest yet significant changes of 10% or more, including the interstitial formation entropy ΔS_f ($0.16k_B$ increase), and extended defect dissociation energy E_{disso} (0.4 eV increase). These changes in parameters yield a significant improvement in the objective function, which decreases from its prior optimized value of 9.9×10^6 to 1.8×10^6.

As an alternate means of evaluation, composite parameters derived from Table 1 may be compared to their counterparts determined via an independent analytical approach.[20] This approach employs an analytical solution of the continuum

https://dx.doi.org/10.1021/acs.langmuir.0c02195
Langmuir 2020, 36, 12632−12648

Table 1. Initial and Final Microkinetic Parameters for O_i

parameter	definition	initial value	final estimate
ΔH_f	enthalpy of O_i formation	3.8 eV	3.6 ± 0.2 eV
ΔS_f	entropy of O_i formation	1.1 k_B	1.26 ± 0.06 k_B
E_{diff}	hopping barrier of bulk O_i	0.65 eV	0.59 ± 0.03 eV
D_0	hopping prefactor of bulk O_i	6.0×10^{-1} cm^2 s^{-1}	(3.0 ± 0.15) cm^2 s^{-1}
E_{inj}	injection barrier	1.2 eV	1.28 ± 0.05 eV
ν_{inj}	injection prefactor	1.0×10^6 s^{-1}	$(1.5 \pm 0.1) \times 10^5$ s^{-1}
E^*_{diss}	barrier to liberate O_i from bulk extended defects	3.3 eV	3.7 ± 0.18 eV
A^*_{diss}	prefactor to liberate O_i from bulk extended defect	2.0×10^{13} s^{-1}	$(8.8 \pm 0.4) \times 10^{12}$ s^{-1}
N_{sat}	saturation concentration of injection sites	1.5×10^{14} cm^{-2}	$(1.6 \pm 0.1) \times 10^{14}$ cm^{-2}
S_0	zero-coverage annihilation probability of O_i	1.5×10^{-5}	$(1.0 \pm 0.05) \times 10^{-5}$

*Other values are possible that satisfy $A_{diss}\exp\left(-\frac{E_{diss}}{k_B T}\right) < (90\ \text{min})^{-1}$

differential equations for defect-mediated diffusional spreading. Detailed analysis of the relative merits of these two forms of mesoscale modeling appears elsewhere.[7,8,13]

The activation energy E_{diss} and prefactor A_{diss} for liberation from extended defects lead to sequestration time constants that are longer than the diffusion time (90 min) in the experiments over the entire temperature range. This result also suggests that any combination of E_{diss} and A_{diss} leading to such long time constants would suffice to reproduce the profiles. In essence, the optimization algorithm employed values of these parameters that affected the profiles, but the iteration scheme converged to a set of values wherein E_{diss} and A_{diss} no longer exerted such effects. The short-time limit actually implies such a lack of influence. Different initial values of these parameters could have evolved to different combinations of E_{diss} and A_{diss} exerting similarly negligible effects. Thus, although the values shown in Table 2 represent reasonable values for these

Table 2. Activation Energies for Composite Parameters for O_i Estimated by Direct Analytical Fitting[1,2] and the Current and Previous[14] Microkinetic Models

	activation energy (eV)	
parameter	analytical[1,2]	microkinetic (previous estimate)[14]
F	1.92 ± 0.27	1.88 ± 0.09 (2.13 ± 0.09)
λ	0.28 ± 0.26	0.31 ± 0.02 (0.39 ± 0.05)
D_{eff}	2.22 ± 0.33	2.19 ± 0.11 (2.52 ± 0.05)

parameters (based upon the "typical" initial value of the prefactor), numerous other combinations exist that would be equally consistent with the experimental data.

Table 2 shows the activation energies for F, λ, and D_{eff} from the microkinetic and analytical approaches. As discussed elsewhere,[7] the microkinetic values exhibit considerably smaller confidence intervals than the analytical ones because of differences in the method of data aggregation. The microkinetic approach assigns more weight to data points having smaller standard deviations and fits the entire data set at the same time. The analytical approach assigns no explicit weighting factor to any data point, and profile-by-profile data aggregation weights each profile equally. Thus, data points from profiles with fewer concentration samplings (e.g., shallower) are implicitly over-represented. The activation energies and prefactors in Table 2 agree quite closely with each other, and the ranges encompassed by the confidence intervals overlap. Figure 2 presents the results for D_{eff}

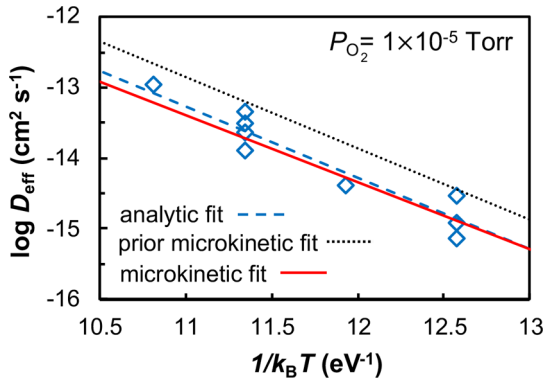

Figure 2. Arrhenius plots of effective diffusivity D_{eff} obtained by analytical and two microkinetic mesoscale models from measured isotope ^{18}O diffusion profiles at T = 650−800 °C and P_{O_2} = 10^{-5} Torr. The current microkinetic model corresponds much more closely to the analytical results.

pictorially through Arrhenius plots. Regardless of the mode of comparison, the present version of the microkinetic model matches the analytical results more closely than previous versions.[8,14]

Useful temperature- and pressure-dependent quantities computed by the present model, such as the coverage θ of injectable species, n, p, and the total concentration of O_i, appear in Figures S1 and S2 in the Supporting Information (SI). The revised model predicts a noticeably higher temperature (nearly 500 K) than that in ref 14 for the transition between the full-coverage regime of $\theta \approx 1$ and the low-coverage regime. Also, the concentration p of holes decreases by 3−4 orders of magnitude due to the larger band gap.

DFT Formation Energies and Geometries. Exchange of O_i in the deep bulk with O_2 gas entails the neutral form of the defect if E_F lies below 0.9 eV and charged −2 for E_F elsewhere in the bandgap. A previous study by this laboratory[11] has examined the identities and thermodynamic formation energies of metastable intermediates along the possible exchange pathways, including the neutral and charged forms of both surface and bulk species.

In accord with prior literature,[11] O_2 adsorption on terraces proved to be energetically unfavorable. This finding aligns with the extensive existing literature examining reduction reactions on TiO_2(110).[35−37] Instead, adsorption and dissociation of O_2 occurs on or near extended surface defects such as step edges. Indeed, scanning probe imaging techniques have demonstrated the ability of O_2 to adsorb dissociatively at ⟨1$\bar{1}$1⟩step edge sites via two distinct channels.[38] Terrace oxygen vacancies probably do not participate because few are likely to exist under the present experimental conditions, and the vacancies act as donors in the +2 charge state,[39] which is unlikely to adsorb molecular oxygen directly. But O atoms produced by O_2 dissociation at edge sites can diffuse to terrace sites, where

https://dx.doi.org/10.1021/acs.langmuir.0c02195
Langmuir 2020, 36, 12632−12648

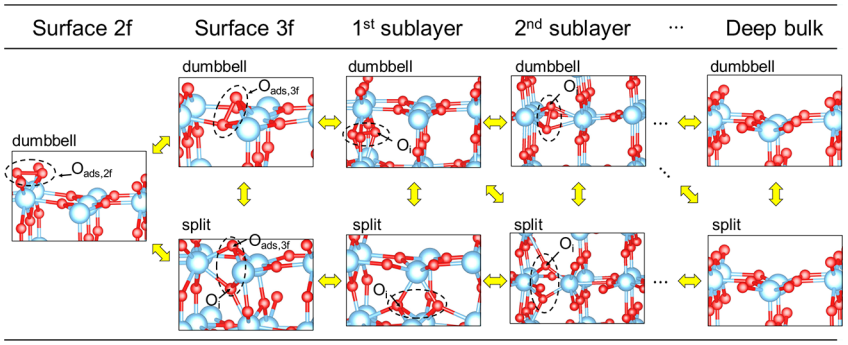

Figure 3. Schematic reaction network for oxygen moving through various sublayers between adsorbed states at the $TiO_2(110)$ surface and the O_i state in the deep bulk. Diagrams depict atomic geometries of key metastable species, and arrows designate the viable routes indicated by DFT for interchange among species. Dumbbell species contain an O−O bond and are always neutral. Split species contain only Ti−O bonds and are always charged −2. Sublayers deeper than the 2nd have properties essentially identical with the deep bulk, as suggested by the three dots.

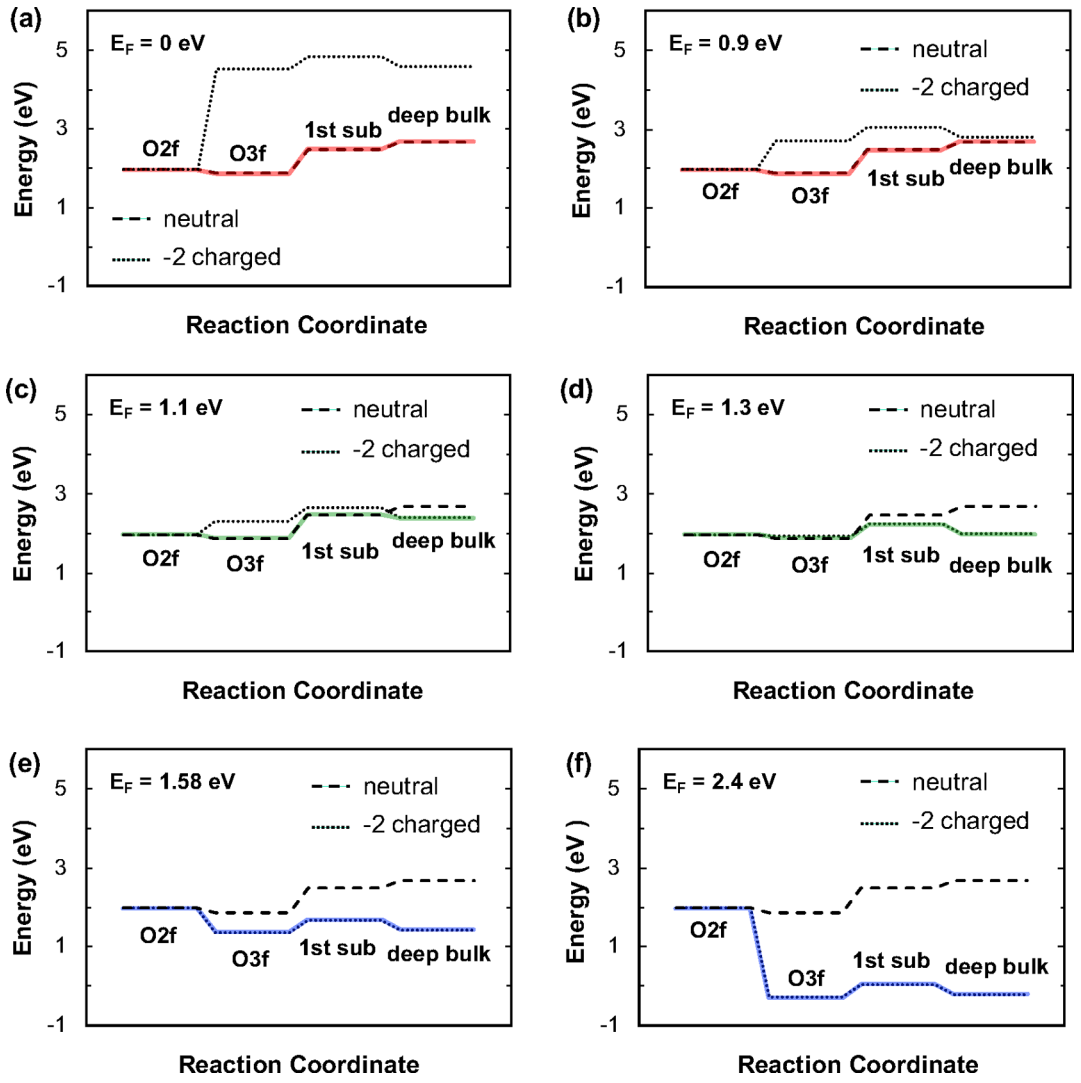

Figure 4. Thermodynamic energy landscape characterizing key metastable species in Figure 3 for representative values of E_F, showing formation energies at the experimental conditions of T = 973 K and P_{O_2} = 1 × 10^{-5} Torr. For ease of reading, the species residing in the 2nd sublayer are omitted, as their energies lie within 0.1 eV of the corresponding deep-bulk species. The landscape for neutral dumbbell species remains invariant with E_F, but the landscape for charged split species changes with E_F; the energies move downward (less positive) as E_F moves up within the bandgap from the VBM to the CBM. Values of E_F corresponding to crossing of the neutral and charged lines for a metastable species correspond to transitions between regimes of E_F shown in later figures.

the adsorbate bonds in either a neutral 2-fold (2f) or a 3-fold (3f) configuration.

The geometry and charge state of the 3f configuration exhibit characteristics that recur repeatedly for the metastable

https://dx.doi.org/10.1021/acs.langmuir.0c02195
Langmuir 2020, 36, 12632−12648

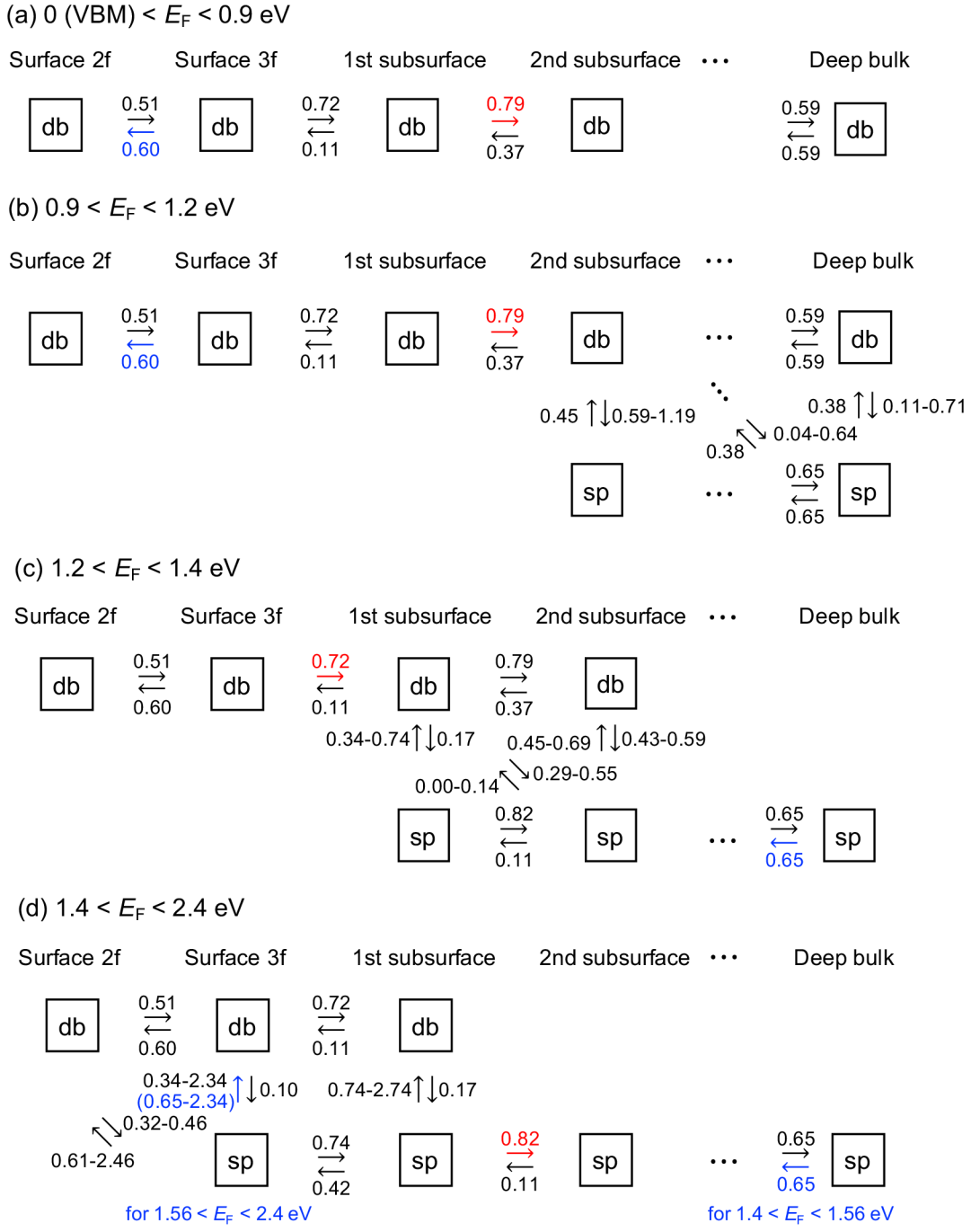

Figure 5. Schematic diagram the reaction pathways that can occur most readily as E_F moves through its domain between the VBM and CBM, based upon the thermodynamic stability of the metastable species. The five metastable states correspond to those in Figure 3, although Figure 3 depicts all stable geometries regardless of E_F. For a given value of E_F, however, not all geometries are stable. For the bandgap of 2.4 eV, four distinct regimes may be defined. The boundaries correspond to values of E_F where crossings occur between formation energies of the neutral dumbbell ("db") and charged split ("sp"). Activation barriers (in eV) are shown for each elementary step, with ranges indicated wherever the barrier varies with E_F within a given regime. Red and blue fonts respectively indicate the rate-determining steps for injection and annihilation in nonequilibrium situations. Sublayers deeper than the 2nd have properties essentially identical with the deep bulk, as suggested by the three dots.

states that mediate oxygen exchange deeper in the bulk. Both on the surface (3f) and within the bulk, the states exist either in neutral dumbbell form with an O−O bond or in charged (−2) split form with only O−Ti bonds. For each metastable state, the dominant form depends upon E_F. Figure 3 summarizes the identities of the most important metastable states as a function of depth within the TiO_2, with arrow signifying which states interconvert with each other as described in detail below. The figure also shows the geometries for neutral dumbbells and the equivalent diagrams for charged split species.

Figure 4 shows thermodynamic energy landscapes involving the metastable states for example values of E_F, described in more detail in elsewhere.[11] The neutral $O_{2f,ads}$ species provides a convenient point of departure for the reaction coordinate because this species participates in all injection and

https://dx.doi.org/10.1021/acs.langmuir.0c02195
Langmuir 2020, 36, 12632−12648

annihilation sequences. Figure 4 presents the formation energies referenced to $E(TiO_2) + 1/2\ \mu_{O_2}$. $E(TiO_2)$ represents the energy of the pristine TiO_2 slab and μ_{O_2} is the O_2 chemical potential[40] at experimental temperature and pressure (T = 973 K and $P_{O_2} = 1 \times 10^{-5}$ Torr).[1,2,7,14] The landscape remains invariant with E_F for neutral dumbbell species, but changes with E_F for charged split species. For the latter, energies shift downward (less positive) as E_F moves up within the bandgap from the VBM to the conduction band minimum (CBM). Consequently, increasing values of E_F provide progressively larger advantages to charged species, and conversion from the neutral dumbbell to the charged split occurs progressively closer to the surface.

Values of E_F corresponding to crossings in Figure 4 of neutral and charged lines represent boundaries between regimes of E_F shown in later figures. For the bandgap of 2.4 eV characterizing the experimental temperature, four regimes may be defined separated by three boundaries. These boundaries involve the surface O_{3f} species (1.4 eV), first or second sublayer (1.2 eV), or bulk O_i (0.9 eV). Additional regimes may be defined in principle by including other boundaries (*e.g.*, at 1.33 eV where the first sublayer split becomes more favorable than its sister dumbbell species). However, the boundaries chosen here suffice to describe the key features of the reaction network. For both dumbbell and split configurations, formation energies converge to about 0.1 eV of the deep-bulk value in the second sublayer. This difference lies at the limit of DFT accuracy, so we considered defect configurations in the third sublayer or deeper as equivalent to the deep bulk.

DFT Barriers within the Reaction Network. Figure 5 schematizes the reaction pathways that can occur most readily as E_F moves through its domain between the VBM and CBM, based upon the thermodynamic stability of the metastable species. Near the edge of a given regime of E_F, the neutral dumbbell and charged split species within one of the sublayers become nearly degenerate in energy. Figure 5 also shows kinetic barriers computed for the elementary steps shown, with Tables 3, 4, 5, and 6 offering summaries of the numerical values in a different form. For a given elementary step, the tables indicate the range of E_F wherein the step participates most actively in the injection or annihilation sequence. Some barriers exhibit a change in their dependence upon E_F within the range where the step participates. The tables contain two entries for such steps showing both functional forms for the E_F dependence and the ranges of E_F over which those forms apply.

Table 3. Elementary Kinetic Steps and Barriers for Injection of Neutral O_i

elementary kinetic step	barrier (eV)
surface diffusion from O_{2f} to O_{3f}	0.51
surface split hopping from O_{3f} into 1st sublayer	0.72
hopping from 1st sublayer into 2nd sublayer	0.79
hopping in deep bulk	0.59

Table 4. Elementary Kinetic Steps and Barriers for Annihilation of Neutral O_i

elementary kinetic step	barrier (eV)
surface diffusion from O_{3f} to O_{2f}	0.60
hopping from 1st sublayer to O_{3f}	0.11
hopping from 2nd sublayer to 1st sublayer	0.37
hopping in deep bulk	0.59

Table 5. Elementary Kinetic Steps and Barriers for Injection of Charge-Assisted O_i

elementary kinetic step	E_F (eV)	barrier (eV)
surface split formation from O_{2f}	1.4–1.47	3.26–2E_F
	1.47–2.4	0.32
surface split formation from O_{3f}	1.4–2.4	0.10
surface split hopping into 1st sublayer	1.4–2.4	0.74
hopping into split from dumbbell at 1st sublayer	1.2–2.4	0.17
hopping into 2nd sublayer split from 1st sublayer dumbbell	1.2–1.33	2.95–2E_F
	1.33–1.4	0.29
hopping into split from dumbbell at 2nd sublayer	0.9–1.28	2.99–2E_F
	1.28–1.4	0.43
hopping from the 1st sublayer into 2nd sublayer	1.4–2.4	0.82
hopping into deep bulk split from above the nearest neighbor sublayer dumbbell	0.9–1.2	2.44–2E_F
hopping into split from dumbbell in deep bulk	0.9–1.2	2.51–2E_F
hopping into split from split in deep bulk	0.9–2.4	0.65

Table 6. Elementary Kinetic Steps and Barriers for Annihilation of Charge-Assisted O_i

elementary kinetic step	E_F (eV)	barrier (eV)
hopping from surface split to O_{2f}	1.4–1.47	0.61
	1.47–2.4	2E_F–2.33
hopping from surface split to O_{3f}	1.4–2.4	2E_F–2.46
hopping from 1st sublayer to surface split	1.4–2.4	0.42
hopping into dumbbell from split at 1st sublayer	1.2–2.4	2E_F–2.06
hopping into 1st sublayer dumbbell from 2nd sublayer split	1.2–1.33	0.00
	1.33–1.4	2E_F–2.65
hopping into dumbbell from split at 2nd sublayer	0.9–1.28	0.45
	1.28–1.4	2E_F–2.11
hopping from 2nd sublayer to 1st sublayer	1.4–2.4	0.11
hopping into the nearest neighbor sublayer dumbbell from deep bulk split	0.9–1.2	0.38
hopping into dumbbell from split in deep bulk	0.9–1.2	0.38
hopping into split from split in deep bulk	0.9–2.4	0.65

For some steps shown in Figure 5, the critical value of E_F for which the barrier switches between E_F-dependent and constant values lies within the regime of E_F where the participating species play important roles in the injection or annihilation sequence. The corresponding arrows therefore show a range of barriers within that regime of E_F. For other steps, the critical value of E_F lies outside the interval of significant participation, so the arrows show only the constant barriers.

For most regimes of E_F, interconversion between a neutral dumbbell and a charged split occurs via two different routes

https://dx.doi.org/10.1021/acs.langmuir.0c02195
Langmuir 2020, 36, 12632–12648

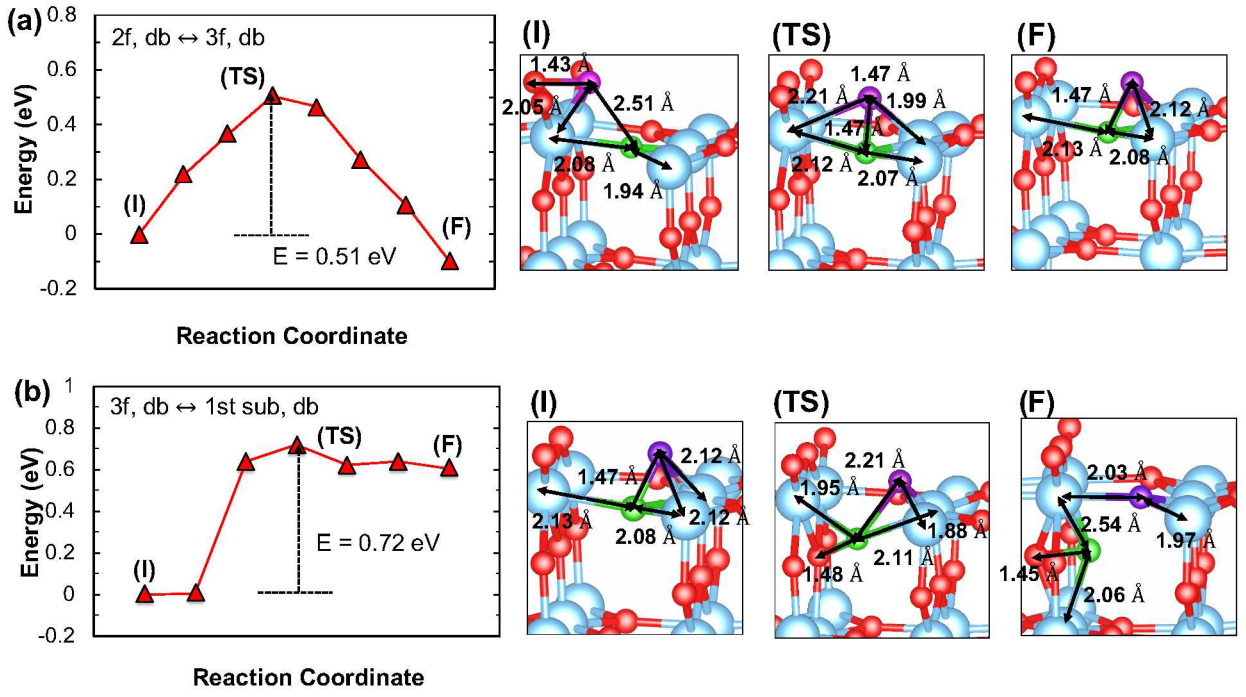

Figure 6. Activation barrier diagrams with corresponding geometries at key points along the reaction coordinate for interchange between neutral dumbbell species at the surface, including (a) 2f ↔ 3f and (b) 3f ↔ 1st sublayer. Rightward movement along the reaction coordinate corresponds to the injection process; leftward corresponds to annihilation. For convenience, key geometries corresponding to initial (I), transition (TS), and final (F) states are referenced to an injection process rather than to annihilation. Blue and red spheres, respectively, designate titanium and lattice oxygen atoms. Green and purple spheres designate key participating O atoms. The numbers next to black arrows denote bond lengths or distances between sites.

that operate in parallel. In one route, the dumbbell and split species reside at the same depth. Vertical arrows represent such routes in Figure 5, and they contribute significantly to the reaction network only near the edges of an E_F regime where both the dumbbell and split exist in appreciable concentrations. In a second route, the dumbbell resides one sublayer closer to the surface than the split. Diagonal arrows represent such routes in Figure 5.

Classes of Barrier Crossings. Examination of Figure 5 and the tables reveals three primary classes of interconversions: dumbbell ↔ dumbbell, split ↔ split, and dumbbell ↔ split. Each class exhibits a distinctive form of behavior when the barrier is crossed. The following paragraphs describe such behavior for each class, with representative examples shown that occur in the near-surface region that comprises the primary focus of this work.

Figure 6a,b show two examples of conversions between neutral dumbbell species: 2f ↔ 3f adsorbates on the surface and 3f ↔1st-sublayer. The participating metastable species exchange no electrons with the conduction band, and the value of E_F exerts no effect upon the barrier height. The transition state occurs about midway along the reaction coordinate between the initial state and final state. Since the experiments measure the appearance (i.e., injection) of isotopic label into the crystal, the activation barrier diagrams employ a convention that defines the initial and final states based on an injection sequence rather than annihilation.

Figure 7a,b show two examples of transitions between charged split species: 3f ↔ first-sublayer and first-sublayer ↔ second-sublayer. The species remain in the same −2 charge state, and exchange no electrons with the conduction band. The value of E_F again exerts no effect upon the barrier height. The transition state occurs late along the reaction coordinate, very near the final state that lies further along the injection sequence than the initial state. Or put another way, the final state lies deeper in the bulk than the initial state.

Figure 8a,b,c show examples of transitions between neutral dumbbell and charged split species: 2f dumbbell ↔ 3f split adsorbates, 3f dumbbell ↔ 3f split adsorbates, and first-sublayer dumbbell ↔ first-sublayer split. In all these cases, the adsorbate or defect changes its charge state during the transition by donating or withdrawing electrons from the conduction band states as described in ref 11. As a result of this electron exchange with the conduction band, the value of E_F influences the energy of any charged species that exist along the reaction coordinate. Therefore, the barrier for the reverse reaction moving toward annihilation invariably depends upon E_F. Interestingly, both the transition state and sometimes the switch between neutral and charged species occurs fairly early along the reaction coordinate (i.e., near the neutral initial state). In some cases, such as 2f dumbbell ↔ 3f split, the position of the transition state shifts rightward (away from the initial state) for a narrow range of E_F before moving back to the original position. The barrier for injection rises in this range. For the case of 2f dumbbell ↔ 3f split in Figure 8a, this movement of the transition state occurs between 1.4 and 1.47 eV. The altered transition state exhibits a slightly evolved geometry consistent with its position further along the reaction coordinate.

Most Favorable Pathways. The preferred pathway through the complicated network depicted in Figures 3 and 5 depends upon how closely the TiO_2 approaches equilibrium with O_2 in the gas phase. When equilibrium prevails (or the quasi-equilibrium that characterizes rutile with slowly evolving

https://dx.doi.org/10.1021/acs.langmuir.0c02195
Langmuir 2020, 36, 12632−12648

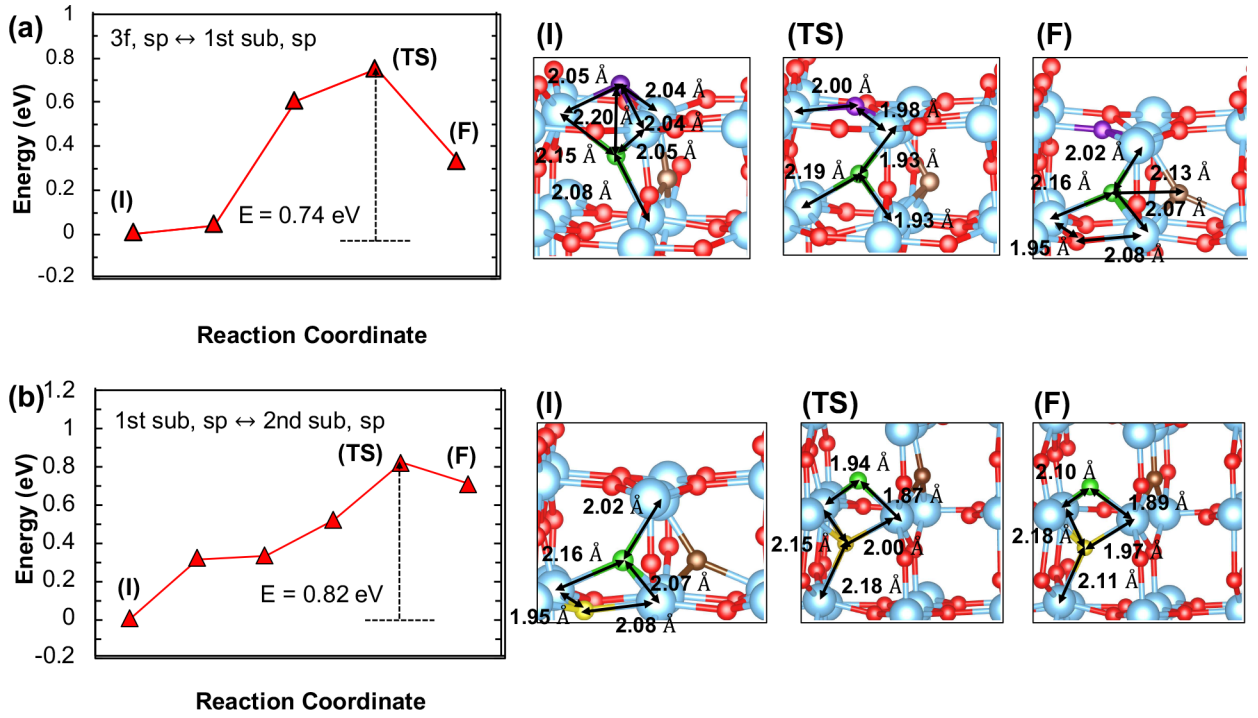

Figure 7. Activation barrier diagrams with corresponding geometries at key points along the reaction coordinate for interchange involving charged split species at the surface. In (a), the charge remains −2 throughout the 3f ↔ 1st sublayer interchange. In (b), charge remains −2 through the 1st sublayer ↔ 2nd sublayer interchange. Rightward movement along the reaction coordinate corresponds to the injection process; leftward corresponds to annihilation. For convenience, key geometries corresponding to initial (I), transition (TS), and final (F) states are referenced to an injection process rather than to annihilation. Blue and red spheres respectively designate titanium and lattice oxygen atoms. Green, purple, brown, yellow spheres designate key participating O atoms. Note that the final-state split configuration in the 2nd sublayer retains considerable asymmetry. Although the lower (yellow) O atom of the split bonds to Ti below it with a length of 2.11 Å, the corresponding distance between the upper (green) O atom and the Ti_{5f} above it is so long (2.61 Å) that no bond is shown. This form of asymmetry disappears rapidly as the oxygen defect sinks deeper into the 3rd and 4th sublayers. The numbers next to black arrows denote bond lengths or distances between sites.

extended defects[41]), the forward and reverse rates for interchange between two metastable species must equal each other, and the rate-limiting step for injection and annihilation must be the same. Far from equilibrium where net injection or net annihilation dominates, the species concentrations readjust so that the step having the highest barrier becomes rate-limiting. These steps may differ for injection and annihilation.

Figure 5 provides the primary barrier information needed to examine the nonequilibrium case. Within each regime of E_F, examination of the elementary-step barriers yields the sequence of steps having the lowest maximum barrier. The largest barrier within that sequence represents the rate-limiting barrier. Figure 9 shows plots of this rate-limiting barrier as a function of E_F for both injection and annihilation.

For injection, the rate-limiting barrier remains within a narrow band only 0.1 eV wide, mostly near 0.8 eV, even though the rate-limiting step varies with E_F. The barrier remains constant at 0.79 eV for $0 < E_F < 1.2$ eV, and entails hopping of the neutral dumbbell from first to second sublayer. The barrier falls discontinuously to 0.72 eV for $1.2 < E_F < 1.4$ eV, and involves hopping from the 3f dumbbell to the first sublayer dumbbell. The barrier rises back to 0.82 eV for $1.4 < E_F < 2.4$ eV, and entails hopping of the charged split from the first to second sublayer.

For annihilation, the rate-limiting barrier exhibits much more variation, especially at large values of E_F. The barrier remains constant at 0.60 eV for $0 < E_F < 1.2$ eV, governed by surface diffusion of adsorbed O from the 3f neutral dumbbell to the 2f neutral dumbbell. The barrier rises discontinuously to 0.65 eV for $1.2 < E_F < 1.56$ eV, and entails hopping of charged O_i^{2-} within the bulk. Finally, the barrier rises linearly from 0.65 to 2.34 eV over the range $1.56 < E_F < 2.4$ eV, and involves conversion from the 3f split to the 3f dumbbell.

The present isotopic labeling experiments are effectively at chemical equilibrium, with the concentrations of metastable species given by thermodynamics (e.g., Figure 4). The rate for a given elementary step is proportional to both a rate constant and a species concentration. The rate scales as $\exp(-E_{barrier}/kT)$, where $E_{barrier}$ denotes the barrier for the step, and k and T respectively represent Boltzmann's constant and temperature. The concentration scales as $\exp(-\Delta H_f/kT)$, where ΔH_f denotes the formation energy of the metastable reactant, given in Figure 4. Thus, the metric $E_{barrier} + \Delta H_f$ serves as a useful measure of the rate, with higher values of the metric signifying lower rates. Figure 10 plots this metric for each pair of steps in Figure 5 for example values of E_F within each of the four regimes. The most active sequence in each regime exhibits the lowest maximum value of $E_{barrier} + \Delta H_f$ (i.e., has the fastest rates throughout the sequence). The particular step within in this sequence having the highest value of $E_{barrier} + \Delta H_f$ limits the rate.

Figure 10 shows that the rate limiting step in equilibrium varies considerably from regime to regime of E_F. As E_F increases from the VBM, the rate limiting step changes from site hopping of deep-bulk dumbbell O_i, to deep-bulk split ↔ second sublayer dumbbell, to second sublayer split ↔ first sublayer dumbbell, to second sublayer split ↔ first sublayer split.

https://dx.doi.org/10.1021/acs.langmuir.0c02195
Langmuir 2020, 36, 12632−12648

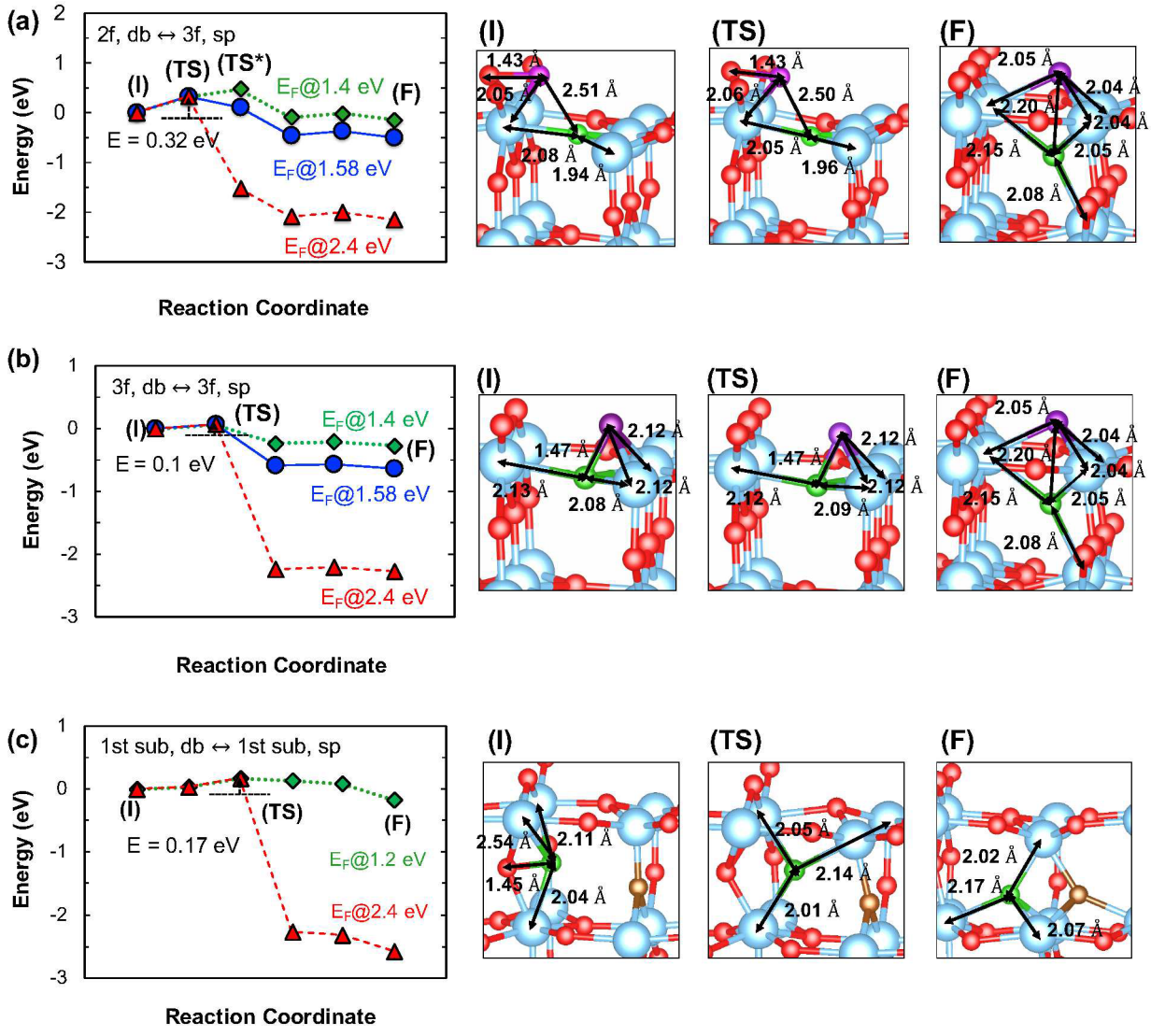

Figure 8. Activation barrier diagrams with corresponding geometries at key points along the reaction coordinate for interconversion to split from dumbbell. Because no charged analog exists for the adsorbed 2f neutral dumbbell, (a) depicts the 2f, dumbbell ↔ 3f, split interchange wherein the charge state switches between neutral and −2, (b) the interchange 3f, dumbbell ↔ 3f, split, and (c) interchange 1st subsurface dumbbell ↔ 1st subsurface split. Rightward movement along the reaction coordinate corresponds to the injection process; leftward corresponds to annihilation. For convenience, key geometries corresponding to initial (I), transition (TS), and final (F) states are referenced to an injection process rather than to annihilation. Blue and red spheres respectively designate titanium and lattice oxygen atoms. Green, purple, brown spheres designate key participating O atoms. In (a), the transition state moves rightward from TS to TS* for a narrow range of E_F between 1.4 and 1.47 eV, with a slightly different geometry (not shown in (a)). The numbers next to black arrows denote bond lengths or distances between sites.

DISCUSSION

Point defect injection and annihilation rates at semiconductor surfaces have been measured reliably within only about the past 15 years. Mathematical expressions for quantifying the rates have been phenomenological, typically conceiving both injection and annihilation as one-step elementary kinetic processes. Rate expressions were often assumed to operate by analogy to Langmuir kinetics for adsorption and desorption of gases (Figure 1), without explicit microscopic justification based on independent experimental or computational methods. One published study indicates that annihilation of silicon interstitials by Si(100) does not obey such Langmuir kinetics, but involves a precursor state with high lateral mobility.[42] The present microkinetic model paired with DFT calculations enables a much more extensive evaluation of Langmuir assumptions for TiO_2(110).

At the chemical (not isotopic) equilibrium assumed to describe a typical isotopic exchange experiment between gas and solid, the rates of defect injection and annihilation at the surface equal each other. For injection, assumption of first-order kinetics leads to the following Langmuir-like rate expression:

$$r_{inj} = k_{inj} n_{sat} \theta \tag{2}$$

where n_{sat} denotes the areal concentration of sites where injection or annihilation takes place. Those sites contain injectable species with a fractional coverage θ. The injection rate constant k_{inj} obeys:

$$k_{inj} = \nu_{inj} e^{-E_{inj}/k_B T} \tag{3}$$

with an activation energy E_{inj} and pre-exponential factor ν_{inj}. For annihilation in the absence of surface poisoning by foreign

https://dx.doi.org/10.1021/acs.langmuir.0c02195
Langmuir 2020, 36, 12632−12648

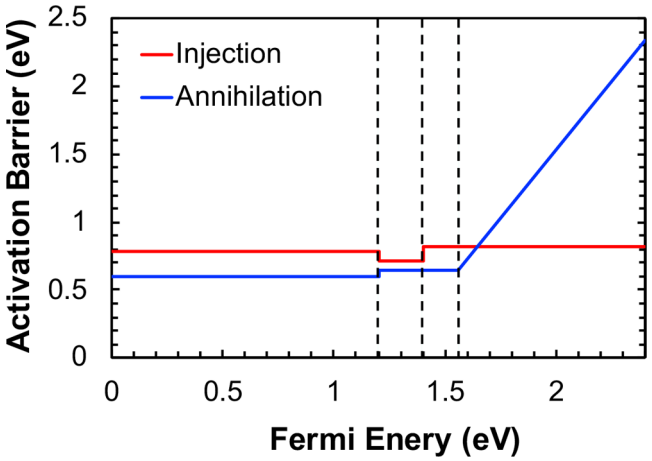

Figure 9. Summary of activation energies for the rate-limiting steps for O_i injection and annihilation at the $TiO_2(110)$ surface. Activation barriers (in eV) are shown as a function of E_F from 0 (VBM) < E_F < 2.4 eV (CBM). Barriers for the rate-determining steps for injection and annihilation are represented in red and blue, respectively.

elements, the rate expression is assumed to obey a Langmuir-like rate expression incorporating the impinging flux and the sticking probability, written as

$$r_{ann} = \frac{3DS_0}{l}(1-\theta)C_{x=0} \quad (4)$$

where D denotes the diffusivity of the defect, S_0 is the zero-coverage sticking probability, l the jump length of the defect, and $C_{x=0}$ the concentration of the defect adjacent to the surface plane.

None of these expressions explicitly incorporates interchange between injectable oxygen and the gas phase through adsorption or desorption. The observed time constants for gas-surface exchange of oxygen on $TiO_2(110)$ are many orders of magnitude smaller than that for exchange of O_i with the surface.[43−48] This observation suggest that adsorption and desorption kinetics of the gas may be safely neglected in when modeling oxygen exchange as described above.

Concept of Injectable Oxygen in Discrete Sites. Figures 3, 7, and 8 indicate that both injection and annihilation entail a multistep sequence involving the in-plane surface split species. Identification of the species corresponding to "injectable oxygen" in eqs 2−4 becomes murky, as the sequence does not map neatly onto a simple three-state picture involving gaseous O_2, adsorbed injectable O, and O_i in the bulk. The adsorbate occupies both O_{2f} and O_{3f} sites that differ by only 0.1 eV in energy and interconvert readily at experimental temperatures. Exchange of oxygen with the TiO_2 bulk involves movement through metastable species in the first and second sublayers that resemble the corresponding bulk species but have thermodynamic energies and hopping barriers that differ from bulk values.

Visual inspection of the atomic geometries in Figure 3 suggests that "injectable oxygen" corresponds to the total oxygen present in O_{3f} sites (dumbbell and split), with O_{2f} oxygen forming an additional reservoir. Once occupied, such O_{3f} sites are "filled" and cannot be occupied by additional O diffusing from other surface sites or from O_i below. This assumption of discrete sites being filled or empty does fit a Langmuir model, albeit with the slight complication of a second 2f adsorption site.

That said, the rate-determining steps for both injection and annihilation vary with E_F and sometimes lie in the second sublayer or deeper, complicating this correspondence. Perhaps it is better to identify the injectable oxygen as the species just upstream of the rate-determining step. This criterion permits the injectable species to change as a function of E_F. However, the results in Figures 5 and 10 show that the rate-limiting step varies depending whether the system is at equilibrium. Out of equilibrium at some values of E_F (including the experiments described here), application of this criterion points to different metastable species for injection and annihilation. Such an ambiguity occurs for the experimental conditions of E_F = 1.58 eV, where the criterion points to O in the first sublayer from the perspective of injection, but the O_{3f} surface split from the perspective of annihilation. Similar ambiguities crop up at other values of E_F.

Yet another possible criterion identifies injectable oxygen as the species in the sequence having the highest concentration. Thermodynamic calculations of free energies could resolve the question, but would require both the enthalpies and entropies of formation to be relevant at the high temperatures characteristic of exchange experiments. First-principles computation of reliable formation entropies requires considerable effort,[10] and the present work did not attempt such computations.

These considerations show that the concept of injectable oxygen may have limited use in systems such as $TiO_2(110)$. The surface split or dumbbell offer the most intuitive candidates, although the coexistence of these two forms near E_F = 1.4 eV and the ready interconversion with $O_{ads,2f}$ and with O_i in the first sublayer complicates the matter.

Interpretation of Microkinetic Activation Energies. Figure 3 shows the kinetic sequence for the charge-assisted oxygen exchange between the gas and bulk. Although all sequences involve neutral $O_{ads,2f}$, Fermi energies above 0.9 eV entail charge exchange between dumbbell and split species that takes place progressively closer to the plane of the $O_{ads,2f}$ as E_F rises. In fact, charge exchange involves two elementary steps that proceed in parallel: one involving direct interconversion between a dumbbell closer to the $O_{ads,2f}$ plane and a split species lying slightly deeper, and the other involving indirect conversion via a dumbbell species that lies at about the same depth as the split. The relative contributions of the two parallel dumbbell ↔ split pathways depends upon E_F in two ways: through the E_F-dependent barriers themselves (Tables 5 and 6), and through the E_F-dependent concentrations of the metastable species involved (governed by eq 1 and energies like those in Figure 4. The former effect yields the complicated dependence of the activation energy for the rate-limiting step shown in Figure 9.

The latter effect acts as follows. The concentrations of neutral and (−2) charge states obey the usual laws of Fermi−Dirac statistics and mass action. Neglecting degeneracy factors arising from electron spin and overlapping band states, the concentration $[A^{2-}]$ of an acceptor state with charge (−2) varies according to[49]

$$[A^{2-}] = [A_{total}]/(1 + \exp(2(E_A - E_F)/kT)) \quad (5)$$

where $[A_{total}]$ represents the total concentration of the relevant acceptor species including all charge states, E_A denotes the acceptor's ionization level. E_A indicates the value of the Fermi energy where the neutral and charged forms of the acceptor have equal concentrations. When E_A and E_F lie very close to

https://dx.doi.org/10.1021/acs.langmuir.0c02195
Langmuir 2020, 36, 12632−12648

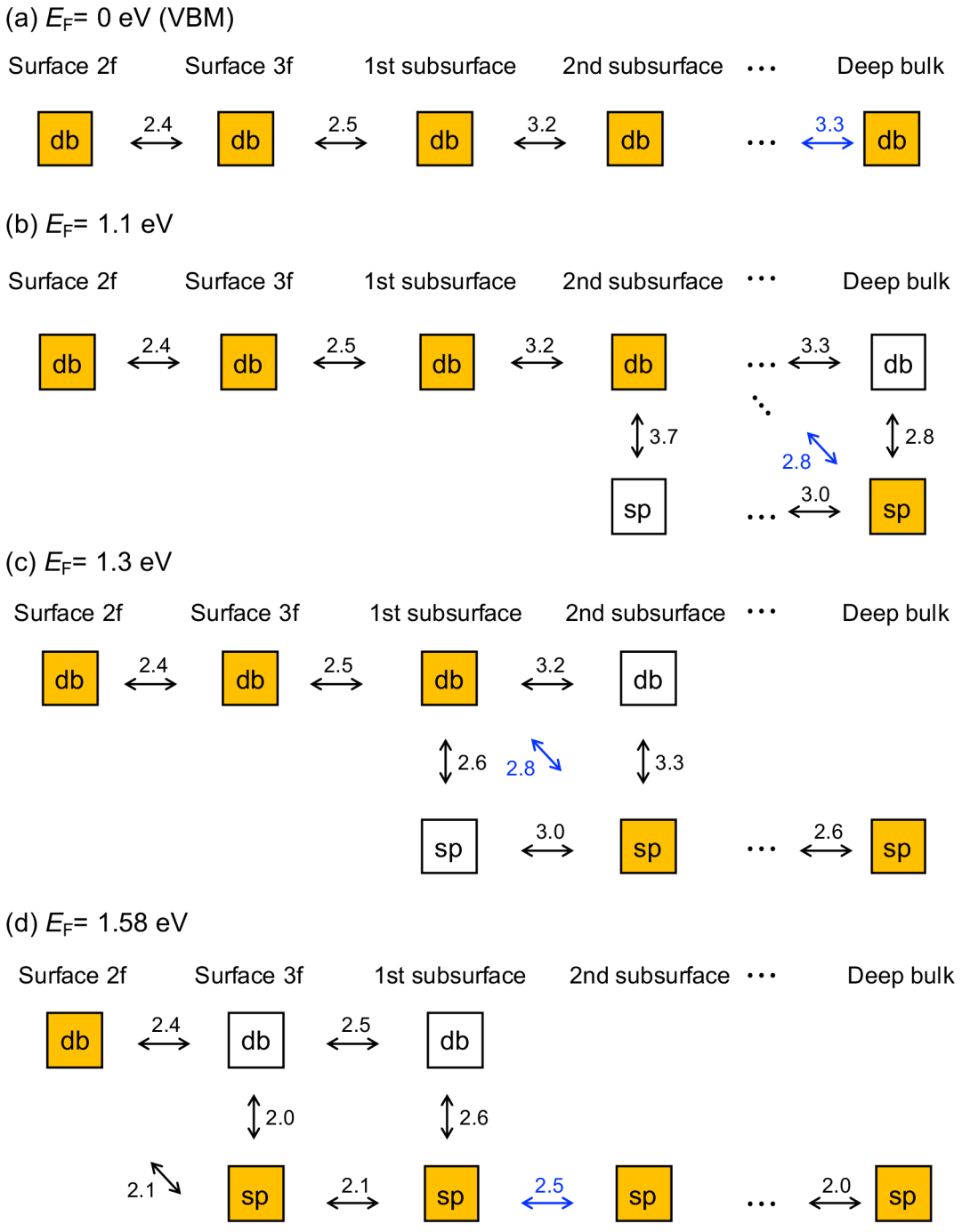

Figure 10. Schematic diagram of Figure 5 redrawn with the rate metric $E_{barrier} + \Delta H_f$ for each forward−reverse pair of elementary steps. For ease of reading, example values of E_F within each regime are shown to avoid the need to depict algebraic expressions of $E_{barrier} + \Delta H_f$ as a function of E_F. The most active sequence in each case exhibits the lowest maximum value of $E_{barrier} + \Delta H_f$ (i.e., has the fastest rates throughout the sequence). The particular step within in this sequence having the highest value of $E_{barrier} + \Delta H_f$ limits the rate at equilibrium, and is indicated with a blue font. These steps of this schematic diagram correspond to the geometries in Figure 3. The notation "db" and "sp" presents O_i dumbbell and split configuration, respectively. Colored boxes signify metastable species that serve as the primary conduits for injection or annihilation under equilibrium conditions. Sublayers deeper than the 2nd have properties essentially identical with the deep bulk, as suggested by the three dots.

each other, appreciable concentrations of both charge states exist simultaneously so that multiple kinetic pathways transpire in parallel. In these transition regions the measured activation energy represents a concentration-weighted aggregation that rounds the sharp breaks in Figure 9 into smooth functions of E_F with continuous values and derivatives. Variations in T alter the concentrations and change the nature of the smoothing.

This physical picture implies that, at a minimum, parameters like E_{inj} and D in the Langmuir-like expressions of eqs 2 and 3 must be formulated to show an explicit dependence upon E_F. Even with that provision, the expressions may fail in many cases because the concentrations of metastable species that contribute to the effective activation energy will themselves change with T. Thus, the weighting factors contributing to the effective values of E_{inj} and D will exhibit a temperature

https://dx.doi.org/10.1021/acs.langmuir.0c02195
Langmuir 2020, 36, 12632−12648

dependence near transition regions of E_F, and thereby contribute to an additional temperature dependence that Figure 9 does not take into account.

Direct Comparison to Experiment: Temperature Dependence of Injection Rate Constant. The modest value of E_{inj} (1.28 eV) constitutes a notable result of the modified microkinetic model. From DFT, none of the elementary steps for injection has a barrier above 1 eV at the temperature and pressure conditions of interest. Thus, the DFT results argue strongly against the large activation energy of 2.4 eV yielded by earlier microkinetic modeling,[7,8,14] as well as the "typical" prefactor assumed in that work of 10^{13} s^{-1}.

Yet E_{inj} still lies roughly 0.45 eV above the barrier of 0.82 eV for the rate-determining step of hopping from the first sublayer to the second sublayer. We speculate this additional temperature dependence arises from variations in the concentration of O atoms just upstream of the rate-determining step.

Figure 2 suggests how to estimate this variation. The surface split has the lowest thermodynamic energy of all the relevant species in the injection sequence and therefore has the highest concentration of O atoms. The split species in the first sublayer lies 0.4 eV higher in energy. Thus, the concentration of oxygen in this sublayer relative to the surface split should increase with temperature according to $\exp(-0.4\ \text{eV}/kT)$. If θ in eq 2 refers to the concentration of oxygen in the first sublayer, then the temperature dependence in k_{inj} incorporates not only the barrier of the rate-determining step (0.82 eV) but also the additional 0.4 eV characterizing the concentration of oxygen in the first sublayer. The total temperature dependence therefore equals the sum of these numbers, meaning 1.22 eV, which matches the experimental value quite closely.

Direct Comparison to Experiment: Temperature Dependence of Annihilation Rate Constant. Equation 4 indicates that two distinct rate constants influence the temperature dependence of r_{ann}: D and S_0. The temperature dependence of D is quantified by E_{diff} = 0.59 eV from the microkinetic model (Table 1), which lies near the values of 0.65 eV from DFT.[10] Derivation of eq 4 presupposes that S_0 is independent of temperature by neglecting surface-induced lattice distortions that bias the direction of bulk hopping near the surface.[50] In other words, a bulk interstitial is assumed to hop toward the surface until it reaches a critical depth where it either hops back into the bulk with a likelihood of $^1/_2$ or proceeds with equal probability to annihilate. The existence of several layers near the surface with hopping barriers below E_{diff} does not substantially undercut this assumption.

For systems out of equilibrium where annihilation dominates, Figure 9 shows that the activation energy for annihilation lies significantly above E_{diff} when E_F > 1.56 eV. The premise underlying eq 4 would therefore fail in this range. S_0 should then be reformulated to incorporate an effective activation energy that depends upon E_F. Otherwise, the microkinetic simulations presuppose no activation energy within S_0, and the fitting procedure would erroneously shift the temperature dependence into other parameters in an ill-defined way. For the present experiments at equilibrium, Figures 5 and 10 show that the rate-limiting step for annihilation involved movement of O from the second to the first sublayer with a barrier of 0.11 eV. Thus, the premise underlying eq 4 remains satisfied.

Pre-Exponential Factors for Injection and Annihilation. The microkinetic model yields a counterintuitively small value of ν_{inj} ($\sim 10^5$ s^{-1}) compared to the typical value of 10^{12}–10^{13} s^{-1} for a typical elementary first-order process. Given the known injection fluxes that lie between 10^{12} and 10^{14} atoms cm^{-2} s^{-1}, this finding follows naturally from the injection barrier below 1 eV indicated by both the microkinetic model and the NEB barrier calculations. O_i injection from $TiO_2(110)$ thereby resembles Ti_i injection in this respect, for which modest injection barriers E_{inj} on the order of 0.5 eV have already been observed experimentally[51] and computationally.[3] Microkinetic modeling of that system has hinted that the corresponding pre-exponential factor is uncommonly low,[8] although no specific value was determined.

The current microkinetic model also yields a notably small value for S_0. S_0 quantifies diffusion-limited hopping to a concentration of surface sites n_{sat} that is comparable to the concentration of surface O atoms. A value of S_0 near unity might therefore be expected, but the actual value lies near 10^{-5}.

Perhaps these low parameters for injection and annihilation arise from surface characteristics specific to TiO_2. In gas desorption, for example, small activation energies and pre-exponential factors can arise for both semiconductors and metals,[52,53] with effects occasionally becoming more pronounced at high adsorbate coverages.[53] Such effects remain only partially explained, but their existence suggests that related phenomena could occur for interstitial injection.

That said, the lack of conceptual registry between the complicated defect exchange sequence shown in Figure 5 and a simple Langmuir-like picture more likely accounts for the anomalously low parameters. The kinetic expressions embodied by eqs 2–4 only approximate the actual expressions, and inadequacies in this approximation will skew some of the parameters.

Interpretation of Barriers in Charge Transfer Steps. The effect of charge transfer on the barrier is accounted for by the number of electrons exchanged with the conduction band and by the relative Fermi level offset between the real-system Fermi energy and DFT-computed Fermi level. We ascertained the number of exchanged electrons via examination of the Bader charges and density of states. The relevant equations and descriptions appear elsewhere.[11]

The barriers in some steps for both surface and bulk diffusion of O exhibit a direct dependence upon E_F. The dependence is linear. These cases represent the first examples in the bulk and surface diffusion literature for semiconductors in which the elementary-step barrier itself varies with E_F due to charge transfer during hopping, distinct from well-known systems where the effective activation energy varies with E_F due to a changing balance in the relative contributions of charge states having different (yet constant) elementary-step barriers.

That said, the barriers in Figure 3 for the steps associated with charge transfer show no obvious patterns that correlate with depth or the direction of reaction (injection or annihilation). The barriers vary from substantial values on the order of 2.5 eV down to negligibly small values (0–0.04 eV). Reactions without barriers are certainly no novelty in chemistry;[54−56] indeed, many forms of dissociative adsorption on surfaces exhibit no barrier despite the breaking of chemical bonds. However, low barriers seem surprising for thermally activated atomic rearrangements in a semiconductor.

As indicated in the Results, the transition state tends to occur early along the reaction coordinate (defined in the injection direction) for dumbbell ↔ split conversions, midway for dumbbell ↔ dumbbell, and late for split ↔ split.

https://dx.doi.org/10.1021/acs.langmuir.0c02195
Langmuir 2020, 36, 12632−12648

Examination of Figures 7 and 8 show that early transitions correspond to very exothermic conversions, and late transitions correspond to very endothermic conversions. This behavior represents a solid-state manifestation of Hammond's postulate from physical organic chemistry.[57,58] That postulate relies upon the notion that, if a transition state and a metastable state have nearly the same energy content, their interconversion requires only a small change in the atomic positions. The geometric depictions in Figures 7 and 8 support this idea.

Curiously, there exists no pathway for direct interchange between the surface 3f neutral dumbbell and the first subsurface charged split (Figure 5d). The interchange occurs only via the first subsurface neutral dumbbell or the 3f charged split. Deeper in the bulk or in the surface plane, exchange between neutral dumbbell and charged split species occurs via two parallel pathways. One pathway involves motion of the O defect between sublayers, and the other involves rebonding of the O defect within a given sublayer.

Examination of the geometries of the relevant metastable species indicates why the 3f dumbbell ↔ first sublayer split interconversion represents an exception; the 3f split metastable state lies near the likely trajectory. The 3f charged split exhibits considerably more asymmetry than other split species deeper in the bulk. As shown in Figures 7a and 8c, the "lower" O atom resembles a bulk split O atom by bonding to two Ti atoms in the surface plane and one Ti atom in a different plane—the second sublayer. However, the "upper" O atom in the split bonds to three Ti atoms that all lie within the surface plane. A consequence of this asymmetry becomes clear by examining the atomic trajectories characteristic of the interconversions of 3f dumbbell ↔ first sublayer dumbbell (Figure 6b) and first sublayer dumbbell ↔ first sublayer split (Figure 8c). Both atoms in the neutral dumbbell would traverse paths in a hypothetical O_{3f} neutral dumbbell ↔ first sublayer split transition that bring them close to positions characteristic of the O_{3f} surface split. Analogous transitions that occur deeper (e.g., involving the first sublayer neutral dumbbell and second sublayer split (Figures 8c (I) and 7b (F))) do not involve a close approach to a metastable state.

The first-principles method employed here to represent charge transfer faces a potential weakness. For each elementary step in which charge transfer takes place, only two NEB calculations are performed: one for the neutral (dumbbell) species and one for the charged (split) species. The method incorporates Fermi level effects via an energy offset applied algebraically for the charged species along the entire reaction coordinate. The energies of the neutral and charged forms of the defect geometry are then compared point-by-point along the reaction coordinate, and the form lying lower in energy is selected as the most stable species. Charge transfer is assumed to occur instantaneously at the location along the reaction coordinate where the energy curves for the neutral and charged species cross. In principle, the atomic geometries of the neutral and charged species could differ appreciably, leading to an artificial discontinuity in the calculated atomic motion along the reaction coordinate at the point where charge transfer takes place.

To test for this weakness, we performed NEB calculations to compare the interconversions 2f dumbbell ↔ 3f dumbbell and 2f dumbbell ↔ 3f split. Figures 6a and 8a already represent these transitions, but SI Figure S3 shows them with a larger number of points along the respective reaction coordinates. Near E_F = 1.4 eV, where the 3f dumbbell and split species have comparable formation energies, the two interconversions proceed in parallel with comparable rates. The energetic trajectories of the two pathways track each other closely, especially near E_F = 1.4 eV for which the transition states have nearly identical energies. Examination of the geometries in SI Figure S3 along the two reaction coordinates show that the trajectories diverge slowly. Thus, the NEB calculations probably reflect a genuine physical reality. Near E_F = 1.4 eV, a mobile O_{2f} atom may start along either of two very similar trajectories that occur with comparable likelihood. One trajectory leads to the 3f neutral dumbbell (through transition state denoted TS** in SI Figure S3), while the other leads to a 3f charged split (through transition state TS* in SI Figure S3). For the split, charge transfers fairly early along the reaction coordinate (between the points labeled TS and TS*) where the atomic geometry still closely resembles that at point S2 on the trajectory leading to the dumbbell. At this point, differences in the geometries for the trajectories leading to the different charge states remain small. This nearly negligible difference reinforces confidence that the calculation method can handle charge transfer without introducing large artificial discontinuities in motion.

Point Defect Manipulation by Fermi Energy. The present results show that kinetic barriers and the rate-determining step vary with E_F for injection and annihilation when the charge state of the bulk defect differs from that of the adsorbate. Furthermore, a notable asymmetry characterizes the activation energies for annihilation and injection. For injection, the barrier remains roughly constant with E_F. In contrast, the barrier for annihilation becomes large (and Fermi level-dependent) when E_F approaches the CBM. This asymmetry represents the kinetic manifestation of a related thermodynamic effect: transferring electrons from the conduction band to the defect becomes easier as the semiconductor becomes more n-type. Indeed, the equilibrium concentration of O_i^{2-} increases as E_F moves toward the conduction band.[7,14]

Several methods have been reported to change E_F at the surface intentionally. For example, gap states introduced by surface point defects have been predicted by DFT[4] to influence E_F strongly, and such effects have been reported experimentally.[59,60] Some bulk dopants change the value of E_F at the surface,[61−63] as can certain adsorbates.[64−66] Creation of heterojunction structures between very thin TiO_2 and a different underlying semiconductor with controllable doping enables some control over E_F at the TiO_2 surface.[67] Combinations of methods, such as Ar bombardment followed by exposure to an oxygen plasma and annealing, varies E_F at the surface over a wide range.[68] Virtually all these approaches affect not only the surface Fermi energy but also some other aspect of the material that influences the diffusion-reaction network for O_i. For example, bulk doping may create new sequestration sites not accounted for in the present model. Heteroatom adsorbates may poison surface sites against injection and annihilation. Heterojunction formation creates a solid−solid interface near the surface that may itself create or annihilate O_i.

The present work does not seek to offer a comprehensive model to account for such phenomena, but does highlight the influence of E_F on the rate limiting step and its energetics. This advance by itself is significant, and will hopefully motivate the development of more comprehensive mathematical models.

https://dx.doi.org/10.1021/acs.langmuir.0c02195
Langmuir 2020, 36, 12632−12648

CONCLUSION

First-principles calculations together with mesoscale microkinetic modeling for TiO_2(110) have been used to demonstrate how the Fermi energy (E_F) at the surface influences the rate-determining step for both injection and annihilation of O_i. Therefore, the effective activation energies for both processes may be manipulated through intentional control of E_F. Indeed, the first-principles calculations have revealed the first examples in the bulk and surface diffusion literature for semiconductors in which the elementary-step barrier itself varies with E_F due to charge transfer during hopping, At equilibrium, the interconversion of O_i species in the first and second sublayers limits the rate. The effective pre-exponential factors for injection and annihilation are surprisingly low, probably resulting from the use of simple Langmuir-like rate expressions like eqs 2−4 to describe a complicated kinetic sequence. Such expressions serve as imperfect but useful approximations for mesoscale models, although the identity of the injectable species corresponding to θ may be difficult to determine.

Looking to the future, mesoscale models having greater precision can certainly be developed. However, such models almost certainly require introduction of more parameters like formation entropies and pre-exponential factors. Such parameters are difficult to compute from first-principles, and require large sets of high-quality profile data to measure with confidence based upon isotopic exchange experiments. The scientific benefit resulting from the improved precision remains unclear.

ASSOCIATED CONTENT

Supporting Information

The Supporting Information is available free of charge at https://pubs.acs.org/doi/10.1021/acs.langmuir.0c02195.

Supporting Figures S1−S3 that involve equilibrium native defect and carrier concentration, injectable oxygen coverage (θ) as a function of temperature and pressure (P_{O_2}) and its Arrhenius relation, and activation barrier diagrams and geometries (PDF)

AUTHOR INFORMATION

Corresponding Author

Edmund G Seebauer − *Department of Chemical and Biomolecular Engineering, University of Illinois at Urbana−Champaign, Urbana, Illinois 61801, United States;* orcid.org/0000-0002-4722-3901; Email: eseebaue@illinois.edu

Authors

Heonjae Jeong − *Department of Mechanical Science and Engineering, University of Illinois at Urbana−Champaign, Urbana, Illinois 61801, United States;* orcid.org/0000-0003-4452-049X

Elif Ertekin − *Department of Mechanical Science and Engineering, University of Illinois at Urbana−Champaign, Urbana, Illinois 61801, United States;* orcid.org/0000-0002-7816-1803

Complete contact information is available at: https://pubs.acs.org/10.1021/acs.langmuir.0c02195

Notes

The authors declare no competing financial interest.

ACKNOWLEDGMENTS

This work was supported by the U.S. National Science Foundation under grant DMR 17-09327. Computational resources were provided by the Illinois Campus Cluster.

REFERENCES

(1) Hollister, A. G.; Gorai, P.; Seebauer, E. G. Surface-Based Manipulation of Point Defects in Rutile TiO2. *Appl. Phys. Lett.* **2013**, *102* (23), 231601.

(2) Gorai, P.; Hollister, A. G.; Pangan-Okimoto, K.; Seebauer, E. G. Kinetics of Oxygen Interstitial Injection and Lattice Exchange in Rutile TiO2. *Appl. Phys. Lett.* **2014**, *104* (19), 191602.

(3) Mulheran, P. A.; Nolan, M.; Browne, C. S.; Basham, M.; Sanville, E.; Bennett, R. A. Surface and Interstitial Ti Diffusion at the Rutile TiO 2 (110) Surface. *Phys. Chem. Chem. Phys.* **2010**, *12* (33), 9763−9771.

(4) Wen, B.; Yin, W.-J.; Selloni, A.; Liu, L.-M. Defects, Adsorbates, and Photoactivity of Rutile TiO2 (110): Insight by First-Principles Calculations. *J. Phys. Chem. Lett.* **2018**, *9* (18), 5281−5287.

(5) Gaberle, J.; Shluger, A. The Role of Surface Reduction in the Formation of Ti Interstitials. *RSC Adv.* **2019**, *9* (22), 12182−12188.

(6) Yoon, Y.; Du, Y.; Garcia, J. C.; Zhu, Z.; Wang, Z.; Petrik, N. G.; Kimmel, G. A.; Dohnalek, Z.; Henderson, M. A.; Rousseau, R. Anticorrelation between Surface and Subsurface Point Defects and the Impact on the Redox Chemistry of TiO2 (110). *ChemPhysChem* **2015**, *16* (2), 313−321.

(7) Pangan-Okimoto, K. M.; Gorai, P.; Hollister, A. G.; Seebauer, E. G. Model for Oxygen Interstitial Injection from the Rutile TiO2 (110) Surface into the Bulk. *J. Phys. Chem. C* **2015**, *119* (18), 9955−9965.

(8) Gilliard-AbdulAziz, K. L.; Seebauer, E. G. Microkinetic Model for Reaction and Diffusion of Titanium Interstitial Atoms near a TiO2 (110) Surface. *Phys. Chem. Chem. Phys.* **2018**, *20*, 4587−4596.

(9) Nowotny, J. Titanium Dioxide-Based Semiconductors for Solar-Driven Environmentally Friendly Applications: Impact of Point Defects on Performance. *Energy Environ. Sci.* **2008**, *1* (5), 565−572.

(10) Jeong, H.; Seebauer, E. G.; Ertekin, E. First-Principles Description of Oxygen Self-Diffusion in Rutile TiO2: Assessment of Uncertainties Due to Energy and Entropy Contributions. *Phys. Chem. Chem. Phys.* **2018**, *20* (25), 17448−17457.

(11) Jeong, H.; Seebauer, E. G.; Ertekin, E. Fermi Level Dependence of Gas-Solid Oxygen Defect Exchange Mechanism on TiO2 (110) by First-Principles Calculations. *J. Chem. Phys.* **2020**, *153* (12), 124710.

(12) Law, M. E.; Cea, S. M. Continuum Based Modeling of Silicon Integrated Circuit Processing: An Object Oriented Approach. *Comput. Mater. Sci.* **1998**, *12* (4), 289−308.

(13) Li, M.; Seebauer, E. G. Microkinetic Model for Oxygen Interstitial Injection from the ZnO (0001) Surface into the Bulk. *J. Phys. Chem. C* **2018**, *122* (4), 2127−2136.

(14) Gilliard-AbdulAziz, K. L.; Seebauer, E. G. Elucidating the Reaction and Diffusion Network of Oxygen Interstitial Atoms near a TiO2 (1 1 0) Surface. *Appl. Surf. Sci.* **2019**, *470*, 854−860.

(15) Gorai, P.; Hollister, A. G.; Seebauer, E. G. Electrostatic Drift Effects on Near-Surface Defect Distribution in TiO2. *Appl. Phys. Lett.* **2013**, *103* (14), 141601.

(16) Gorai, P.; Seebauer, E. G. Electric Field-Driven Point Defect Pile-up near ZnO Polar Surfaces. *Solid State Ionics* **2017**, *301*, 95−98.

(17) Gunawan, R.; Jung, M. Y. L.; Braatz, R. D.; Seebauer, E. G. Parameter Sensitivity Analysis Applied to Modeling Transient Enhanced Diffusion and Activation of Boron in Silicon. *J. Electrochem. Soc.* **2003**, *150* (12), G758−G765.

(18) Varma, A.; Morbidelli, M.; Wu, H. *Parametric Sensitivity in Chemical Systems*; Cambridge University Press, 2005.

(19) Beck, J. V.; Arnold, K. J. *Parameter Estimation in Engineering and Science*; James Beck, 1977.

(20) Gorai, P.; Hollister, A. G.; Seebauer, E. G. Measurement of Defect-Mediated Oxygen Self-Diffusion in Metal Oxides. *ECS J. Solid State Sci. Technol.* **2012**, *1* (2), Q21−Q24.

(21) Hohenberg, P.; Kohn, W. Inhomogeneous Electron Gas. *Phys. Rev.* **1964**, *136* (3B), B864.
(22) Kohn, W.; Sham, L. J. Self-Consistent Equations Including Exchange and Correlation Effects. *Phys. Rev.* **1965**, *140* (4A), A1133.
(23) Kresse, G.; Furthmüller, J. Efficiency of Ab-Initio Total Energy Calculations for Metals and Semiconductors Using a Plane-Wave Basis Set. *Comput. Mater. Sci.* **1996**, *6* (1), 15−50.
(24) Kresse, G.; Furthmüller, J. Efficient Iterative Schemes for Ab Initio Total-Energy Calculations Using a Plane-Wave Basis Set. *Phys. Rev. B: Condens. Matter Mater. Phys.* **1996**, *54* (16), 11169−11186.
(25) Kresse, G.; Joubert, D. From Ultrasoft Pseudopotentials to the Projector Augmented-Wave Method. *Phys. Rev. B: Condens. Matter Mater. Phys.* **1999**, *59* (3), 1758−1775.
(26) Perdew, J. P.; Burke, K.; Ernzerhof, M. Generalized Gradient Approximation Made Simple. *Phys. Rev. Lett.* **1996**, *77* (18), 3865−3868.
(27) Henkelman, G.; Uberuaga, B. P.; Jónsson, H. A Climbing Image Nudged Elastic Band Method for Finding Saddle Points and Minimum Energy Paths. *J. Chem. Phys.* **2000**, *113* (22), 9901−9904.
(28) Wang, L.; Maxisch, T.; Ceder, G. Oxidation Energies of Transition Metal Oxides within the GGA+U Framework. *Phys. Rev. B: Condens. Matter Mater. Phys.* **2006**, *73* (19), 1−6.
(29) Zhang, Y.; Yang, W. Comment on "Generalized Gradient Approximation Made Simple. *Phys. Rev. Lett.* **1998**, *80* (4), 890.
(30) Kowalski, P. M.; Camellone, M. F.; Nair, N. N.; Meyer, B.; Marx, D. Charge Localization Dynamics Induced by Oxygen Vacancies on the TiO2 (110) Surface. *Phys. Rev. Lett.* **2010**, *105* (14), 146405.
(31) Chen, J.; Li, Y.-F.; Sit, P.; Selloni, A. Chemical Dynamics of the First Proton-Coupled Electron Transfer of Water Oxidation on TiO2 Anatase. *J. Am. Chem. Soc.* **2013**, *135* (50), 18774−18777.
(32) Hebenstreit, E. L. D.; Hebenstreit, W.; Geisler, H.; Thornburg, S. N.; Ventrice, C. A., Jr; Hite, D. A.; Sprunger, P. T.; Diebold, U. Sulfur on TiO2 (110) Studied with Resonant Photoemission. *Phys. Rev. B: Condens. Matter Mater. Phys.* **2001**, *64* (11), 115418.
(33) Stevanovic, A.; Büttner, M.; Zhang, Z.; Yates, J. T., Jr Photoluminescence of TiO2: Effect of UV Light and Adsorbed Molecules on Surface Band Structure. *J. Am. Chem. Soc.* **2012**, *134* (1), 324−332.
(34) Lany, S.; Zunger, A. Assessment of Correction Methods for the Band-Gap Problem and for Finite-Size Effects in Supercell Defect Calculations: Case Studies for ZnO and GaAs. *Phys. Rev. B: Condens. Matter Mater. Phys.* **2008**, *78* (23), 235104.
(35) Onishi, H.; Fukui, K.; Iwasawa, Y. Atomic-Scale Surface Structures of TiO2 (110) Determined by Scanning Tunneling Microscopy: A New Surface-Limited Phase of Titanium Oxide. *Bull. Chem. Soc. Jpn.* **1995**, *68* (9), 2447−2458.
(36) Fischer, S.; Munz, A. W.; Schierbaum, K.-D.; Göpel, W. The Geometric Structure of Intrinsic Defects at TiO2 (110) Surfaces: An STM Study. *Surf. Sci.* **1995**, *337* (1−2), 17−30.
(37) Diebold, U.; Lehman, J.; Mahmoud, T.; Kuhn, M.; Leonardelli, G.; Hebenstreit, W.; Schmid, M.; Varga, P. Intrinsic Defects on a TiO2 (110) (1× 1) Surface and Their Reaction with Oxygen: A Scanning Tunneling Microscopy Study. *Surf. Sci.* **1998**, *411* (1−2), 137−153.
(38) Wen, H. F.; Miyazaki, M.; Zhang, Q.; Adachi, Y.; Li, Y. J.; Sugawara, Y. Direct Observation of Atomic Step Edges on the Rutile TiO 2 (110)-(1× 1) Surface Using Atomic Force Microscopy. *Phys. Chem. Chem. Phys.* **2018**, *20* (44), 28331−28337.
(39) Li, H.; Guo, Y.; Robertson, J. Calculation of TiO2 Surface and Subsurface Oxygen Vacancy by the Screened Exchange Functional. *J. Phys. Chem. C* **2015**, *119* (32), 18160−18166.
(40) Zhang, Y.; Yang, W. Comment on "Generalized Gradient Approximation Made Simple. *Phys. Rev. Lett.* **1998**, *80* (4), 890.
(41) Gilliard, K. L.; Seebauer, E. G. Manipulation of Native Point Defect Behavior in Rutile TiO2 via Surfaces and Extended Defects. *J. Phys.: Condens. Matter* **2017**, *29* (44), 445002.
(42) Zhang, X.; Yu, M.; Kwok, C. T. M.; Vaidyanathan, R.; Braatz, R. D.; Seebauer, E. G. Precursor Mechanism for Interaction of Bulk Interstitial Atoms with Si (100). *Phys. Rev. B: Condens. Matter Mater. Phys.* **2006**, *74* (23), 235301.
(43) Wu, X.; Selloni, A.; Lazzeri, M.; Nayak, S. K. Oxygen Vacancy Mediated Adsorption and Reactions of Molecular Oxygen on the TiO 2 (110) Surface. *Phys. Rev. B: Condens. Matter Mater. Phys.* **2003**, *68* (24), 241402.
(44) Wang, Y.; Pillay, D.; Hwang, G. S. Dynamics of Oxygen Species on Reduced TiO2 (110) Rutile. *Phys. Rev. B: Condens. Matter Mater. Phys.* **2004**, *70* (19), 193410.
(45) Rasmussen, M. D.; Molina, L. M.; Hammer, B. Adsorption, Diffusion, and Dissociation of Molecular Oxygen at Defected TiO2 (110): A Density Functional Theory Study. *J. Chem. Phys.* **2004**, *120* (2), 988−997.
(46) Wendt, S.; Schaub, R.; Matthiesen, J.; Vestergaard, E. K.; Wahlström, E.; Rasmussen, M. D.; Thostrup, P.; Molina, L. M.; Lægsgaard, E.; Stensgaard, I. Oxygen Vacancies on TiO2 (1 1 0) and Their Interaction with H2O and O2: A Combined High-Resolution STM and DFT Study. *Surf. Sci.* **2005**, *598* (1−3), 226−245.
(47) Kimmel, G. A.; Petrik, N. G. Tetraoxygen on Reduced TiO 2 (110): Oxygen Adsorption and Reactions with Bridging Oxygen Vacancies. *Phys. Rev. Lett.* **2008**, *100* (19), 196102.
(48) Chrétien, S.; Metiu, H. O2 Evolution on a Clean Partially Reduced Rutile TiO2 (110) Surface and on the Same Surface Precovered with Au1 and Au2: The Importance of Spin Conservation. *J. Chem. Phys.* **2008**, *129* (7), 74705.
(49) Van Vechten, J. A.; Moss, T. S. A Simple Man's View of the Thermochemistry of Semiconductors. *Handb. Semicond.* **1980**, *3*, 168.
(50) Kwok, C. T. M.; Dev, K.; Braatz, R. D.; Seebauer, E. G. A Method for Quantifying Annihilation Rates of Bulk Point Defects at Surfaces. *J. Appl. Phys.* **2005**, *98* (1), 13524.
(51) Bowker, M.; Bennett, R. A. The Role of Ti3+ Interstitials in TiO2 (110) Reduction and Oxidation. *J. Phys.: Condens. Matter* **2009**, *21* (47), 474224.
(52) Wang, Z.; Seebauer, E. G. Estimating Pre-Exponential Factors for Desorption from Semiconductors: Consequences for a Priori Process Modeling. *Appl. Surf. Sci.* **2001**, *181* (1−2), 111−120.
(53) Seebauer, E. G.; Kong, A. C. F.; Schmidt, L. D. The Coverage Dependence of the Pre-Exponential Factor for Desorption. *Surf. Sci.* **1988**, *193* (3), 417−436.
(54) Li, Y.-F.; Selloni, A. Theoretical Study of Interfacial Electron Transfer from Reduced Anatase TiO2 (101) to Adsorbed O2. *J. Am. Chem. Soc.* **2013**, *135* (24), 9195−9199.
(55) Li, Y.; Gao, Y. Interplay between Water and TiO 2 Anatase (101) Surface with Subsurface Oxygen Vacancy. *Phys. Rev. Lett.* **2014**, *112* (20), 206101.
(56) Bao, J. L.; Zhang, X.; Truhlar, D. G. Barrierless Association of CF2 and Dissociation of C2F4 by Variational Transition-State Theory and System-Specific Quantum Rice−Ramsperger−Kassel Theory. *Proc. Natl. Acad. Sci. U. S. A.* **2016**, *113* (48), 13606−13611.
(57) Hammond, G. S. A Correlation of Reaction Rates. *J. Am. Chem. Soc.* **1955**, *77* (2), 334−338.
(58) Graham Solomons, T. W.; Fryhle, C. B. *Organic Chemistry*, 8th ed.; John Wiley & Sons, Inc., 2004.
(59) Wendt, S.; Sprunger, P. T.; Lira, E.; Madsen, G. K. H.; Li, Z.; Hansen, J. Ø.; Matthiesen, J.; Blekinge-Rasmussen, A.; Lægsgaard, E.; Hammer, B. The Role of Interstitial Sites in the Ti3d Defect State in the Band Gap of Titania. *Science (Washington, DC, U. S.)* **2008**, *320* (5884), 1755−1759.
(60) Nowotny, M. K.; Bogdanoff, P.; Dittrich, T.; Fiechter, S.; Fujishima, A.; Tributsch, H. Observations of P-Type Semiconductivity in Titanium Dioxide at Room Temperature. *Mater. Lett.* **2010**, *64* (8), 928−930.
(61) Graciani, J.; Álvarez, L. J.; Rodriguez, J. A.; Sanz, J. F. N Doping of Rutile TiO2 (110) Surface. A Theoretical DFT Study. *J. Phys. Chem. C* **2008**, *112* (7), 2624−2631.
(62) Nowotny, M. K.; Sheppard, L. R.; Bak, T.; Nowotny, J. Defect Chemistry of Titanium Dioxide. Application of Defect Engineering in Processing of TiO2-Based Photocatalysts. *J. Phys. Chem. C* **2008**, *112* (14), 5275−5300.

https://dx.doi.org/10.1021/acs.langmuir.0c02195
Langmuir 2020, 36, 12632−12648

(63) Yu, Y.; Yang, X.; Zhao, Y.; Zhang, X.; An, L.; Huang, M.; Chen, G.; Zhang, R. Engineering the Band Gap States of the Rutile TiO2 (110) Surface by Modulating the Active Heteroatom. *Angew. Chem., Int. Ed.* **2018**, *57* (28), 8550−8554.
(64) Martinez, U.; Hammer, B. Adsorption Properties versus Oxidation States of Rutile TiO_2(110). *J. Chem. Phys.* **2011**, *134* (19).194703
(65) Müller, M.; Sánchez-Portal, D.; Lin, H.; Brivio, G. P.; Selloni, A.; Fratesi, G. Effect of Structural Fluctuations on Elastic Lifetimes of Adsorbate States: Isonicotinic Acid on Rutile (110). *J. Phys. Chem. C* **2018**, *122* (14), 7575−7585.
(66) Alghamdi, H.; Idriss, H. Study of the Modes of Adsorption and Electronic Structure of Hydrogen Peroxide and Ethanol over TiO2 Rutile (110) Surface within the Context of Water Splitting. *Surf. Sci.* **2018**, *669*, 103−113.
(67) Kazazis, D.; Guha, S.; Bojarczuk, N. A.; Zaslavsky, A.; Kim, H. C. Substrate Fermi Level Effects in Photocatalysis on Oxides: Properties of Ultrathin TiO_2 /Si Films. *Appl. Phys. Lett.* **2009**, *95* (6).064103
(68) Kashiwaya, S.; Morasch, J.; Streibel, V.; Toupance, T.; Jaegermann, W.; Klein, A. The Work Function of TiO2. *Surfaces* **2018**, *1* (1), 73−89.

https://dx.doi.org/10.1021/acs.langmuir.0c02195
Langmuir 2020, 36, 12632−12648